

National and Kapodistrian University of Athens,
Department of Physics Section of Astrophysics, Astronomy
and Mechanics

Coronal properties of Active Galactic Nuclei using a sample of Seyfert I galaxies

Georgios Dimopoulos



July 15, 2019

Committee

Dr. Ioannis Georgantopoulos (*National Observatory of Athens*)

Prof. Apostolos Mastichiadis (*Section of Astronomy and Astrophysics, Dept. of Physics, University of Athens*)

Prof. Despina Hatzidimitriou (*Section of Astronomy and Astrophysics, Dept. of Physics, University of Athens*)

Ευχαριστίες

Η παρούσα εργασία έγινε σε συνεργασία με το Εθνικό Αστεροσκοπείο Αθηνών. Θα ήθελα να ευχαριστήσω τους Γεωργαντόπουλο Ιωάννη και Ακύλα Αθανάσιο για την καθοδήγηση καθώς και τον Angel Ruiz για τη βοήθεια που μου προσέφερε καθόλη τη διάρκεια της εργασίας. Επίσης, θα ήθελα να ευχαριστήσω τον καθηγητή Μαστιχιάδη Απόστολο και την Μπουλά Στέλλα από τον τομέα Αστροφυσικής για τις συμβουλές που μου έδωσαν για την καλύτερη κατανόηση του αντικειμένου.

Abstract

Active Galactic Nuclei (AGN) are among the most exotic objects in the Universe and therefore, their study has always been a challenge for the astrophysicists. In this work, we try to investigate the properties of the corona of the AGN; the hot plasma cloud above the accretion disk that it is responsible for the hard X-ray component of the spectrum. To do so, we study a sample of Seyfert I galaxies and derive the properties of their coronae. Next, we investigate the potential correlation between the coronal properties and intrinsic properties of the AGN. Finally, we show a physical mechanism that can be applied to regulate the environment in these plasma clouds and the conclusions we get from our analysis. In chapter I, we present a brief introduction to AGN, illustrating some of the most common types, their differences and then we show the main components of an AGN and its role in this complex system. The physical mechanisms that form the shape of the spectrum of an AGN are mostly related to High Energy Astrophysics because the outcome is result of interaction between high energy particles and photons. In chapter II, we discuss the fundamental physics of high energy interactions, like Compton Scattering, Inverse Compton Scattering and Comptonization, and eventually present briefly a Generalized Comptonization theory developed in the 90's. Finally, in chapter III, we present our whole analysis and the results.

Περίληψη

Οι Ενεργοί Γαλαξιακοί Πυρήνες (AGN) αποτελούν κάποια από τα πιο εξωτικά αντικείμενα στο Σύμπαν και συνεπώς, η μελέτη τους αποτελεί σημαντικό στόχο για τους αστροφυσικούς. Στην παρούσα εργασία, ερευνούμε τις ιδιότητες της κορώνας των ΕΓΠ. Η κορώνα είναι ένα σύννεφο πλάσματος που βρίσκεται πάνω από τον δίσκο προσαύξησης και είναι υπεύθυνη για το μέρος του φάσματος που αποτελείται από σκληρές ακτίνες Χ. Μελετάμε ένα δείγμα από Seyfert I τύπου γαλαξίες και εξάγουμε τις ιδιότητες της κορώνας σε καθέναν από αυτούς τους γαλαξίες. Στη συνέχεια, αναζητούμε πιθανή συσχέτιση μεταξύ των φυσικών ιδιοτήτων της κορώνας με άλλες ιδιότητες του AGN. Τελικά, παρουσιάζουμε έναν φυσικό μηχανισμό που μπορεί να λειτουργεί ως ρυθμιστής του περιβάλλοντος της κορώνας και παρουσιάζουμε τα συμπεράσματα της εργασίας μας. Συγκεκριμένα, στο πρώτο κεφάλαιο, δίνουμε μία σύντομη εισαγωγή για τα AGN, αναφέροντας τους διαφορετικούς τύπους καθώς και τα μέρη από τα οποία αποτελείται ένα AGN. Έπειτα, παρουσιάζουμε, μερικώς, κάποιες από τις φυσικές διεργασίες που συμβαίνουν σε αυτά τα συστήματα και διέπονται κυρίως από αλληλεπιδράσεις Υψηλών Ενεργειών, όπως Σκέδαση Κόμπτον, Αντίστροφος Σκεδασμός Κόμπτον και Κομπτονισμός. Τέλος, στο τρίτο κεφάλαιο, περιέχεται η ανάλυση που κάναμε καθώς και τα τελικά αποτελέσματα και συμπεράσματα.

Contents

1	Introduction	6
1.1	What is an Active Galaxy	6
1.2	Types of Active Galaxies	8
1.2.1	Active Galaxies with Jets	9
1.2.2	Active Galaxies without Jets	11
1.3	The components of an Active Galactic Nucleus	13
1.3.1	Supermassive Black Hole (SMBH)	14
1.3.2	Accretion Disk	15
1.3.3	Corona	16
1.3.4	Dust torus	17
2	Interactions of High Energy Photons	18
2.1	Compton Scattering	18
2.2	Inverse Compton Scattering	21
2.3	Comptonization	22
2.3.1	The simple physical framework	22
2.3.2	Generalized Comptonization Models	24
3	Analysis	30
3.1	Introduction	30
3.2	The sample	30
3.2.1	Sample	30
3.2.2	Black hole mass	31
3.3	Spectral modeling	32
3.4	Results	33
3.5	Conclusion	39
4	Appendix	41

1 Introduction

1.1 What is an Active Galaxy

Galaxies are massive stellar structures that contain matter in the form of stars, gas regions, molecular clouds and dark matter. If you observe these objects with telescopes you can see different shapes, some have spirals some not, but if your telescope were equipped to examine the spectra of the galaxies, then the active galaxies would stand out.

Normal galaxies contain stars that are generally similar to those in our own Galaxy; and spiral galaxies have additional similarities to the Milky Way in their gas and dust content. Active galaxies show extra emission of radiation, and this is most apparent from the spectra. In Figure (1.1) the non-stellar light from the central region is dominant and this indicates the presence of a powerful emission engine in the nucleus, called Active Galactic Nucleus or AGN in short. As a result, a galaxy that hosts an active nucleus is called Active Galaxy and the nucleus AGN.

As implicit in the name, AGN are stronger emitters than the nuclei of “normal” galaxies. This “extra” component is unrelated to the nuclear fusion powering stars and is now universally accepted to be connected instead to the presence of an actively accreting central supermassive ($\geq 10^6 M_\odot$) black hole (SMBH). AGN are the most powerful non-explosive sources in the Universe with very high luminosities (up to $L_{bol} \approx 10^{48} \text{erg/s}^{-1}$), visible up to very high redshifts (currently $z = 7.5$; Bañados et al., 2018).

AGN can be observed in all spectral bands. In Figure (1.2) (Fig. 1, Padovani et al., 2017) the different components of an AGN spectrum are illustrated. Different methods are employed in different bands to identify these sources but, most importantly, the various wavelength regimes provide different windows on AGN physics. Namely, the infrared (IR) band is mostly sensitive to obscuring material and dust, the optical/ultraviolet (UV) band is related to emission from the accretion disk, while the X-ray band traces the emission of a corona. γ -ray and (high flux density) radio samples, on the other hand, preferentially select AGN emitting strong non-thermal (jet [or associated lobe] related) radiation.

1 Introduction

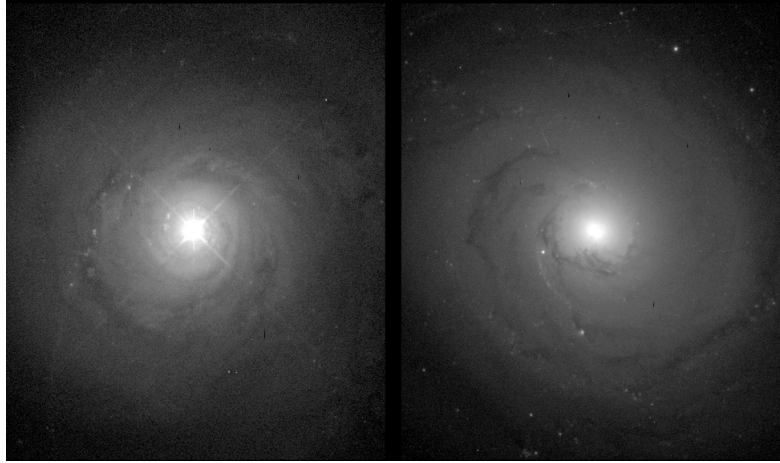


Figure 1.1: Comparison of the active galaxy NGC 5548 (left) and the normal spiral galaxy NGC 3277 (right). Both images have been captured in optical and both galaxies are in the same distance. The nucleus of the active galaxy is significantly brighter and that points out the existence of an AGN.
<http://pages.astronomy.ua.edu/gifimages/ngc5548.html>

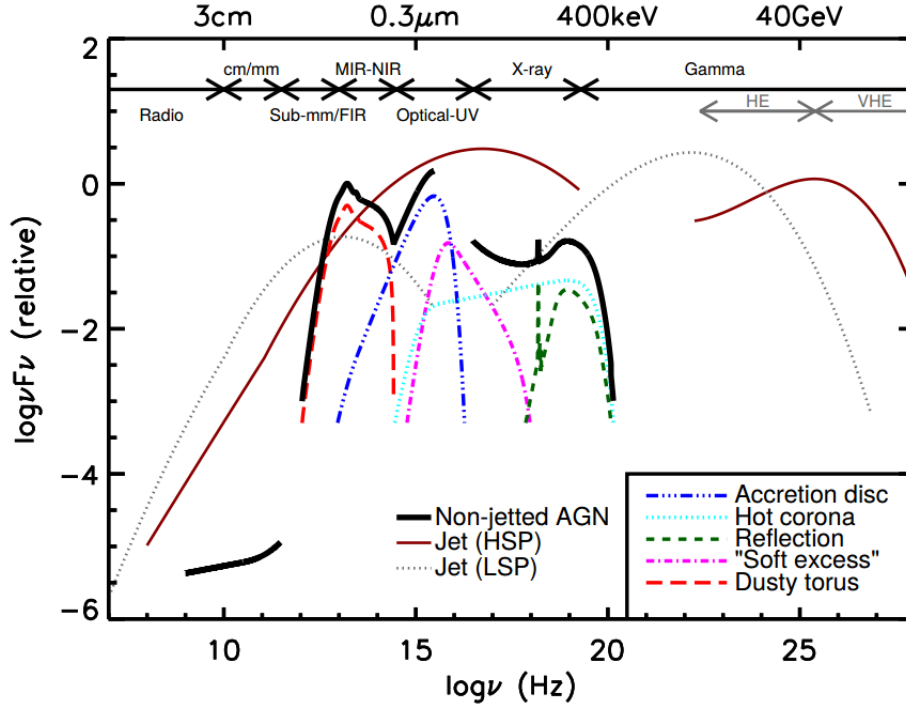


Figure 1.2: A schematic representation of an AGN spectral energy distribution (SED), loosely based on the observed SEDs of non-jetted quasars. The black solid curve represents the total emission and the various coloured curves (shifted down for clarity) represent the individual components. The intrinsic shape of the SED in the mm-far infrared (FIR) regime is uncertain; however, it is widely believed to have a minimal contribution (to an overall galaxy SED) compared to star formation (SF), except in the most intrinsically luminous quasars and powerful jetted AGN. The primary emission from the AGN accretion disk peaks in the UV region. The jet SED is also shown for a high synchrotron peaked blazar (HSP, based on the SED of Mrk 421) and a low synchrotron peaked blazar (LSP, based on the SED of 3C 454.3; . Image credit: C. M. Harrison.

1.2 Types of Active Galaxies

Even though, all AGN have many characteristics in common, like excessive X-ray emission, infrared strong emission, prominent emission lines etc, there are specific traits that help us separate them into distinctive categories. In Padovani et al. (2017) the classification has been made by separating AGN according to the spectrum band observed and the different characteristics that can be found in these bands, like emission lines, variability etc. More than 50 classes can be found in the literature which makes AGN classification naming, puzzling and confusing. However, we will focus on the most frequent and easily recognized classes.

1 Introduction

In order to do so, we will initially separate active galaxies into two main categories; jetted and non-jetted. It is clear that this criterion refers to the presence or absence of a strong relativistic jet. Having done that, some of the most common subclasses will be presented. In Figure (1.3) someone can see an example of an active galaxy with jet (left) and without jet (right).



Figure 1.3: Examples of jetted and non-jetted active galaxies. *Left*: Image of the Radio Loud galaxy Hercules A. The two symmetric jets are prominent and are strong radio emitters (Credits: NASA, ESA, S. Baum and C. O’Dea (RIT), R. Perley and W. Cotton (NRAO/AUI/NSF), and the Hubble Heritage Team (STScI/AURA)). *Right*: An image of the well known Circinus galaxy. A Seyfert II type galaxy captured by HST. (Credits: NASA, Andrew S. Wilson (University of Maryland); Patrick L. Shopbell (Caltech); Chris Simpson (Subaru Telescope); Thaisa Storchi-Bergmann and F. K. B. Barbosa (UFRGS, Brazil); and Martin J. Ward (University of Leicester, U.K.))

1.2.1 Active Galaxies with Jets

Powerful relativistic jets are very common in AGN and therefore Active Galaxies that host such jets can be considered a major category mostly known as jetted AGN (also Radio Loud). However, different properties of these galaxies can lead us to further classification and here the most frequent jetted galaxies are presented.

The major trait that separates jetted galaxies is the observation angle (the line of sight angle). In other words, whether the jet propagation is happening across the line of sight or perpendicular to that. The left galaxy in Figure (1.3) is an example of the latter case. When the jet points towards the earth, the jet itself cannot be distinguished, yet strong synchrotron emission and γ -ray emission can work us proxy to ensure the presence of a relativistic jet, housing ultra-fast electrons.

Two of the most common types of pointing jetted galaxies are BL Lacertae (BL Lac) and Flat Spectrum Radio Galaxy (FSRQ). Both BL Lacs and FSRQs have strong jets and the synchrotron radiation component is prominent in their spectra. Mechanisms such as Self Synchrotron Absorption (SSA) can be found in the low energy part of the synchrotron component. Moreover, Synchrotron Self Compton (SSC) forms a high energy component from X-rays all the way to γ -rays. In Figure (1.4) the spectra of a BL Lac and FSRQ are presented, showing that BL Lacs are, in general, less luminous than FSRQs, probably due to lower Eddington accretion rate.

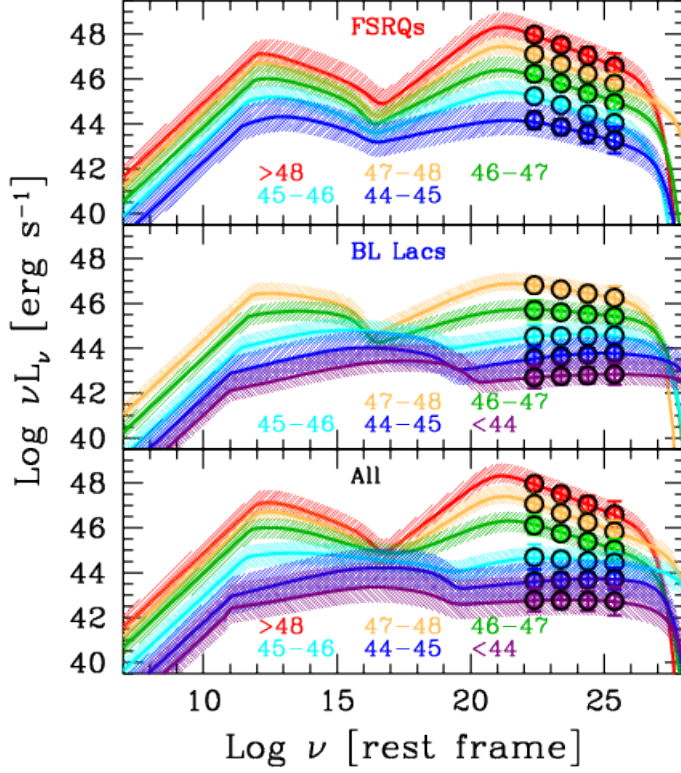


Figure 1.4: Spectra of BL Lacs (mid) and FSRQs (top). The two “humps” are clear with the low energy one being formed by excessive synchrotron emission and the second one by Synchrotron Self Compton (SSC). BL Lacs are less luminous than FSRQs. (Credits: The Fermi blazar sequence - Ghisellini, G. et al. Mon.Not.Roy.Astron.Soc. 469 (2017) no.1, 255-266 arXiv:1702.02571 [astro-ph.HE])

When the propagation of the jet is perpendicular to the line of sight, or at least in high angle, then the actual jet can be observed along with the radio lobes formed in regions far from the central engine, due to collision between the jet and the Interstellar or Intergalactic Medium (ISM, IGM). Well known types of such galaxies are Fanaroff-Riley type I and type II (FRI, FRII). Fanaroff-Riley Class I (FR-I) sources have their low brightness regions further from the central galaxy or quasar than their high brightness regions (see Figure (1.5) left). The sources become fainter as one approaches the outer extremities of the lobes and the spectra here are the steepest, indicating that the radiating particles have aged the most. Jets are detected in 80 per cent of FR-I galaxies. Fanaroff-Riley Class II (FR-II) class comprises luminous radio sources with hotspots in their lobes at distances far from the centre. These sources are called edge-darkened, which

1 Introduction

was particularly apt terminology when the angular resolution and dynamic range used in observing the classical sources was not always good enough to reveal the hotspots as distinct structures. In keeping with the overall high luminosity of this type of source, the cores and jets in them are also brighter than those in FR-I galaxies in absolute terms; but relative to the lobes these features are much fainter in FR-II galaxies (see Figure (1.5) right).

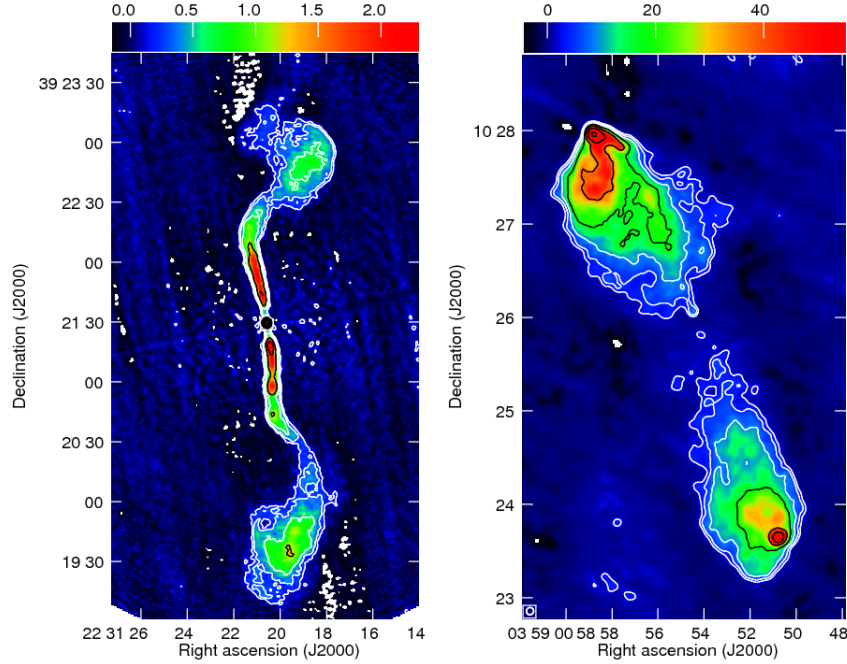


Figure 1.5: Fanaroff-Riley active galaxies. In the left an FR I type galaxy with dominant symmetric jets, while on the right an FR II galaxy with prominent hotspots in radio lobes. (Credits: Understanding Jets from Sources Straddling the Fanaroff-Riley Divide - Kharb, Preeti et al. IAU Symp. 313 (2015) 211-218 arXiv:1411.1534 [astro-ph.GA])

1.2.2 Active Galaxies without Jets

Having seen galaxies with huge jet formations one can relate the powerful jets with high activity in the nucleus, which is correct, but there are AGN without jets with comparable luminosities. Hence, the high activity in the central engine does not mean essentially presence of jet. Two of the most common non-jetted active galaxies are Seyfert galaxies; type I and type II. Seyfert galaxies are named after Carl Seyfert, who first described this class in 1943, and host a very luminous AGN, while the host galaxy (most of the times spiral) is also detectable. They have quasar-like nuclei (very luminous, distant and bright sources of electromagnetic radiation) with very high surface brightnesses whose spectra reveal strong, high-ionisation emission lines. Due to the lack of jet, the spectrum observed

1 Introduction

comes from the central region and therefore it is related to radiation processes near the SMBH, like UV thermal emission, comptonization, reflection etc. The very difference between the two classes (Sy I, Sy II) is the presence or absence of broad emission lines (see Figure (1.6)). Broad emission lines are formed in a region near the SMBH with high radial velocities that shift a narrow emission line in both sides of the spectrum. A Seyfert I galaxy has strong broad emission lines, whereas a Seyfert II does not. This selection criterion is an observational effect and it is related to the inclination of the galaxy along the line of sight. Face on galaxies provide broad lines due to lack of extra material that in Seyfert II hides the central region.

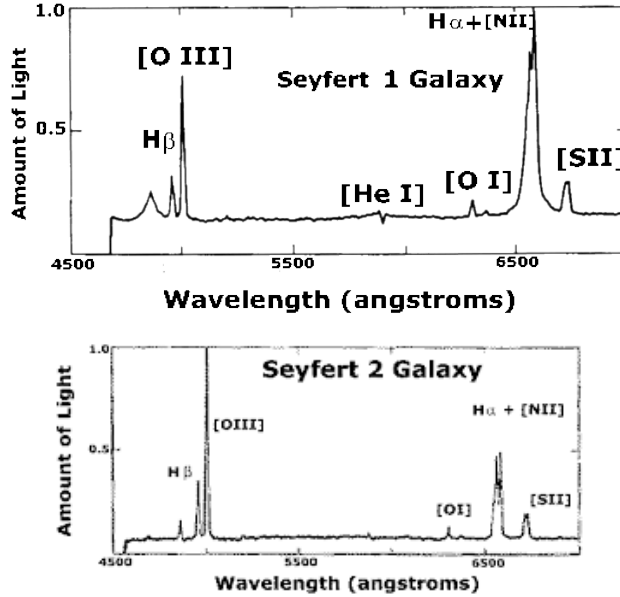


Figure 1.6: Schematic spectra of a Seyfert I galaxy (top) and Seyfert II (bottom). The lack of broad emission lines in Sy II galaxies is the characteristic that separates the two population and it is an observational effect, high or low inclination. (Credits: <http://casswww.ucsd.edu/archive/public/tutorial/AGN.html>)

Finally, a low-ionization nuclear emission-line region (LINER) is a type of galactic nucleus that is defined by its spectral line emission. The spectra typically include line emission from weakly ionized or neutral atoms, such as O, O $^+$, N $^+$, and S $^+$. Conversely, the spectral line emission from strongly ionized atoms, such as O $^{++}$, Ne $^{++}$, and He $^+$, is relatively weak. The class of galactic nuclei was first identified by Timothy Heckman in the third of a series of papers on the spectra of galactic nuclei that were published in 1980. Galaxies that contain LINERs are often referred to as LINER galaxies. LINER galaxies are very common; approximately one-third of all nearby galaxies (galaxies within approximately 20-40 Mpc) may be classified as LINER galaxies. In Figure (1.7) a comparison between a LINER, a Seyfert and an H II region is provided, and it is clear that LINERs are less luminous than Seyferts.

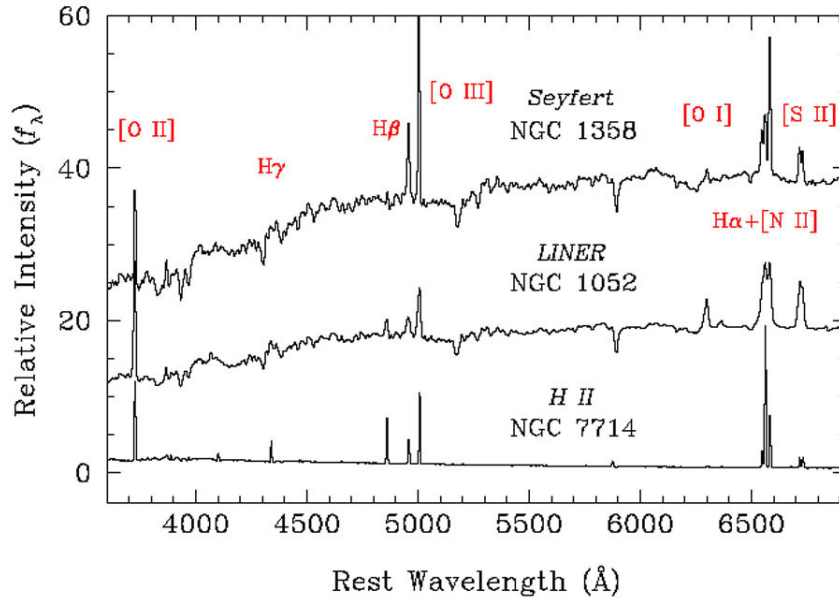


Figure 1.7: Spectra from a LINER, a Seyfert and an H II region presented to compare the luminosity. (Credits: <http://personal.psu.edu/mxe17/A440/materials.html>)

1.3 The components of an Active Galactic Nucleus

According to the unification model that currently describes an AGN, the classification of AGN is based on two criteria. First, the presence or absence of jet and second, the inclination in respect to the line of sight. In Figure (1.8) (Zier and Biermann, 2002), a schematic of the unification model is illustrated. Each Active Galaxy can be divided into two main components; the host galaxy and the central engine. For the purpose of this work, we will focus on the central engine, which is the powerful nucleus. The nucleus consists of four main formations. (i) The Supermassive Black Hole (SMBH), (ii) The Accretion Disk, (iii) The Corona, and (iv) The Torus. Each of these components plays its role in the shape of the spectrum produced.

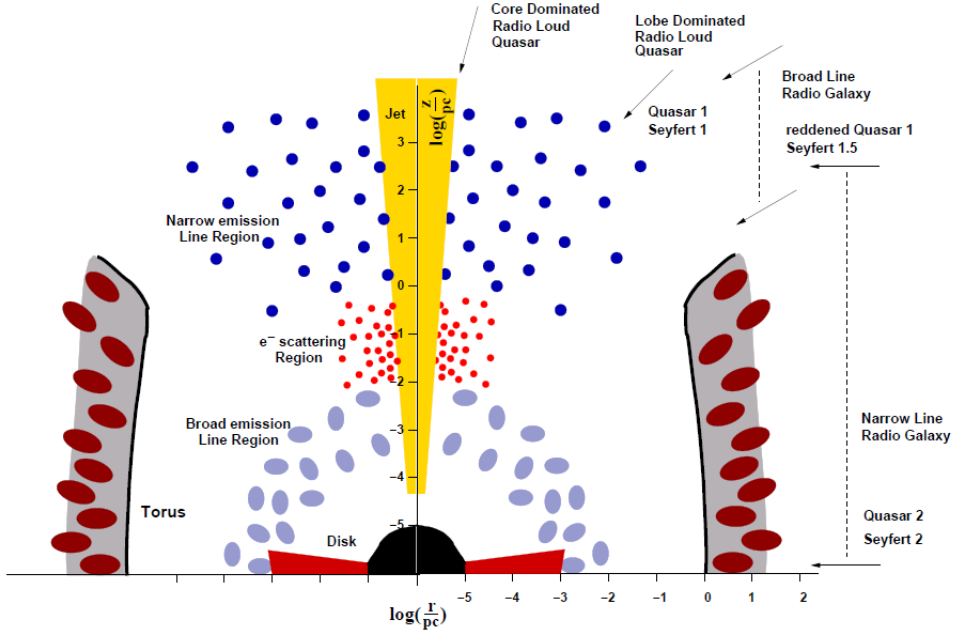


Figure 1.8: The unification model of an AGN. The schematic illustrates the different regions of an AGN, including the classification depending on the line of sight. (Credits: Zier and Biermann, 2002)

1.3.1 Supermassive Black Hole (SMBH)

AGN are hosts of Supermassive Black Holes (SMBH) that are thought to be the outcome of huge merging events in the early universe. Yet, the formation of SMBH so early in the cosmic time is still one of the major mysteries in astrophysics (see Bañados et al., 2018). Knowing more about the SMBH helps us understand better the physics behind such exotic objects. A typical dimension for the black holes is the Schwarzschild radius which is $r_g = 2GM/c^2$. Two of the most important properties are the (i) mass of the SMBH and (ii) the spin. Methods in order to measure the black hole mass have been developed using either the trajectories of stars moving close to the SMBH or the broadening of several emission lines. Such methods are:

- Using velocity dispersion - black hole mass relation proposed by Kormendy and Ho (2013)

$$\log\left(\frac{M_{BH}}{M_{\odot}}\right) = 4.38 \times \log\left(\frac{\sigma_*}{200 \text{ km s}^{-1}}\right) + 8.49 \quad (1.1)$$

- Using single epoch spectra of broad $H\beta$ emission lines (Trakhtenbrot and Netzer, 2012)

$$M_{BH}(H\beta) = 1.05 \times 10^8 \left(\frac{L_{5100}}{10^{46} \text{ erg s}^{-1}}\right)^{0.65} \left[\frac{FWHM(H\beta)}{10^3 \text{ km s}^{-1}}\right]^2 M_{\odot} \quad (1.2)$$

1 Introduction

- Using single epoch spectra of broad $H\alpha$ emission lines (Greene and Ho, 2005)

$$M_{BH}(H\alpha) = 1.3 \times 10^6 \left(\frac{L_{H\alpha}}{10^{42} \text{ergs}^{-1}} \right)^{0.57} \left[\frac{FWHM(H\alpha)}{10^3 \text{km s}^{-1}} \right]^{2.06} M_{\odot} \quad (1.3)$$

Bentz and Katz (2015) used reverberation mapping for all available emission lines and created an AGN Mass catalog¹. The black hole mass for the majority of AGN varies from million to billion solar masses ($10^6 - 10^9 M_{\odot}$) (Koss et al., 2017). In Figure (1.9) a histogram of the black hole mass from the *BAT AGN Spectroscopic Survey (BASS)* is presented, containing sources observed in the *Swift/BAT 70-month AGN Catalog*.

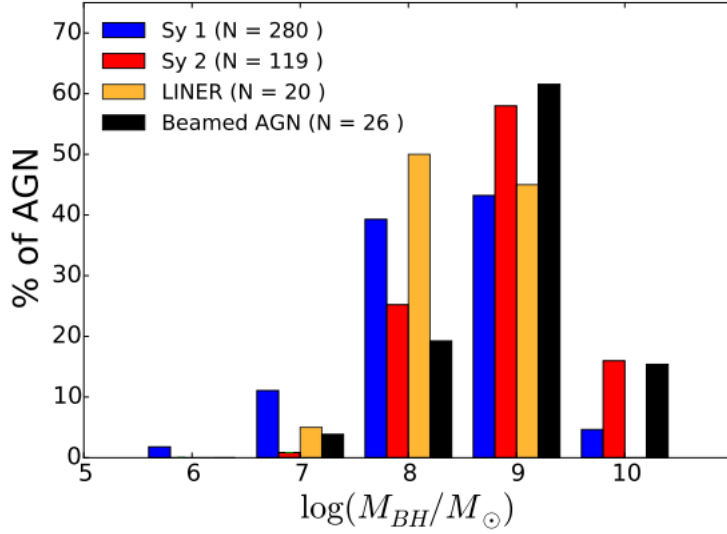


Figure 1.9: Histogram of the black hole mass from Koss et al. (2017).

1.3.2 Accretion Disk

The Accretion Disk around the central black hole is the key emission mechanism in AGN. The photons generated in the accretion disk are those that undergo different physical processes and form the observable spectrum. Accretion Disks are thought to be polychromatic thermal emitters that reach radiation energies up to UV band (Lasota, 2016). A characteristic property of an accretion disk is the Eddington limit luminosity which is found by setting equilibrium between the infalling material (gravity) and the emitting radiation (radiation pressure). Assuming the radiation pressure is provided by photons being scattered on electrons in the Thompson scattering regime, the following calculations can be made:

¹<http://www.astro.gsu.edu/AGNmass/>

1 Introduction

$$F_{grav} = \frac{GM}{r^2}(m_p + m_e) \approx \frac{GMm_p}{r^2} \quad (1.4)$$

For photons with energy $h\nu$ and flux $L/4\pi r^2$ (L the Luminosity and r the distance from the source), the flux density of photons is:

$$N_{photons} = \frac{L}{4\pi r^2 h\nu} \quad (1.5)$$

The force of the photons is related to the momentum transferred from photons to electrons it is given by:

$$F_{rad} = \sigma_T N_{ph} p \quad (1.6)$$

where $\sigma_T = 6.653 \times 10^{-29} m^2$ the Thompson cross-section and $p = h\nu/c$ the photon momentum. Hence, the Eddington luminosity is:

$$\begin{aligned} F_{grav} &= F_{rad} \Rightarrow \\ \frac{GMm_p}{r^2} &= \sigma_T \frac{L_{EDD}}{4\pi r^2} \frac{h\nu}{c} \Rightarrow \\ L_{EDD} &= \frac{4\pi GMm_p c}{\sigma_T} \end{aligned} \quad (1.7)$$

Eddington luminosity describes the maximum luminosity a source of mass M can emit.

1.3.3 Corona

The corona, a hot cloud of electrons close to the centre of the accretion disc, produces the hard X-ray power-law continuum commonly seen in luminous active galactic nuclei. The continuum has a high-energy turnover, typically in the range of one to several 100 keV and is suggestive of Comptonization by thermal electrons. A spherical corona has typical properties of unit Thomson depth, $\tau_T = 1$, temperature $kt = 50keV$ and radius $10r_g$ (Fabian et al., 2017) and according to Merloni and Fabian (2001), the energy supplying the heat must be stored in the corona, probably in the form of magnetic fields powered by the accretion disc. Despite the temperature and the optical depth, a corona can be described by the *dimensionless compactness* which is given by (Guilbert et al., 1983):

$$l = \frac{L}{R} \frac{\sigma_T}{m_e c^3} \quad (1.8)$$

which in terms of gravitational radius and Eddington luminosity is:

$$l = 4\pi \frac{m_p}{m_e} \frac{R_g}{R} \frac{L_{bol}}{L_{EDD}} \quad (1.9)$$

1 Introduction

In this work, the properties of the coronae for a sample of Seyfert I galaxies will be presented, as well as, the potential correlation between the corona and the AGN (see also Fabian et al. (2017); Fabian et al. (2015); Guilbert et al. (1983)).

1.3.4 Dust torus

Current models suggest a toroidal mass of dust and gas that obscures the nucleus from some lines of sight while collimating the radiation that escapes. “Type 1” objects (those with very broad emission lines in their optical spectra) are those in which we have a direct view of the hot, fast-moving material close to the accretion disk. In “type 2” AGN the torus obscures this material, and we see only narrow emission lines in the optical spectrum (Mason, 2015). The torus must be small because it has never been resolved at the $\sim 0''.3$ angular resolution available from large, ground-based telescopes in the mid-IR, even in the nearest AGN. Moreover, it is clumpy which is implied by several lines of evidence, perhaps most intuitively by the X-ray eclipse events observed in several AGN. Detection of Silicate features, seen in emission or absorption around 10 and 20 μm ; The 3.4 μm C-H stretch, produced by aliphatic hydrocarbons in dust grains and observed in absorption; Polycyclic aromatic hydrocarbon (PAH) emission features, such as those at 3.3, 6.2, 7.7, 8.6, 11.3, and 12.7 μm ; and Ice absorption bands, including the 3.0 and 6.0 μm H₂O features prove the presence of solid state molecules (see Mason (2015); Ramos Almeida and Ricci (2017)).

2 Interactions of High Energy Photons

The interaction of High Energy Photons can be summarized in three main processes. The photoelectric absorption, where photons are being absorbed by atoms so as to get ionized; Compton scattering, where photons collide with nuclei or electrons and exchange energy; finally electron - positron pair production, where photons interact with each other and a pair of electron - positron is created. In general, we consider photon from X-rays ($\sim 1keV$) and above as High Energy photons. The processes described above can be found in different environments. We will focus on Compton scattering, Inverse Compton Scattering (ICS) and Comptonization, phenomena which are important for the formation and shape of the spectrum of an AGN and other accreting objects.

2.1 Compton Scattering

Compton scattering can be naively described as the Thompson scattering with energy exchange. In general, as long as the energy of the photon is much less the rest mass energy of the electron ($h\nu \ll m_e c^2$) the collision between a photon and an electron can be considered taking place in the Thompson framework. However, there are cases where the energy exchange and hence the change in the frequency of the photon cannot be neglected.

The momentum four-vectors of an electron and photon before and after the collision are:

	Before	After
Electron	$\mathbf{P} = [\gamma m_e c, \gamma m_e \mathbf{u}]$	$\mathbf{P}' = [\gamma' m_e c, \gamma' m_e \mathbf{u}']$
Photon	$\mathbf{K} = [\frac{h\nu}{c}, \frac{h\nu}{c} \mathbf{i}_k]$	$\mathbf{K}' = [\frac{h\nu'}{c}, \frac{h\nu'}{c} \mathbf{i}'_k]$

The four-momentum must be conserved, so:

$$\mathbf{P} + \mathbf{K} = \mathbf{P}' + \mathbf{K}' \tag{2.1}$$

If we square both sides:

$$(\mathbf{P} + \mathbf{K})^2 = (\mathbf{P}' + \mathbf{K}')^2 \Rightarrow$$

$$\mathbf{P} \cdot \mathbf{P} + 2\mathbf{P} \cdot \mathbf{K} + \mathbf{K} \cdot \mathbf{K} = \mathbf{P}' \cdot \mathbf{P}' + 2\mathbf{P}' \cdot \mathbf{K}' + \mathbf{K}' \cdot \mathbf{K}' \Rightarrow$$

2 Interactions of High Energy Photons

$$\begin{aligned} \cancel{\mathbf{P} \cdot \mathbf{P}} + 2\mathbf{P} \cdot \mathbf{K} + \cancel{\mathbf{K} \cdot \mathbf{K}} &= \cancel{\mathbf{P}' \cdot \mathbf{P}'} + 2\mathbf{P}' \cdot \mathbf{K}' + \cancel{\mathbf{K}' \cdot \mathbf{K}'} \Rightarrow \\ \mathbf{P} \cdot \mathbf{K} &= \mathbf{P}' \cdot \mathbf{K}' \end{aligned} \quad (2.2)$$

we make use of the properties:

$$\mathbf{P} \cdot \mathbf{P} = \mathbf{P}' \cdot \mathbf{P}' = m_e^2 c^2 \quad \text{and} \quad \mathbf{K} \cdot \mathbf{K} = \mathbf{K}' \cdot \mathbf{K}' = 0 \quad (2.3)$$

Now if we multiply (2.1) by \mathbf{K}' and use the equality (2.2) we have:

$$\mathbf{P} \cdot \mathbf{K}' + \mathbf{K} \cdot \mathbf{K}' = \mathbf{P}' \cdot \mathbf{K}' + \mathbf{K}' \cdot \mathbf{K}' \Rightarrow$$

$$\mathbf{P} \cdot \mathbf{K}' + \mathbf{K} \cdot \mathbf{K}' = \mathbf{P}' \cdot \mathbf{K}' + \cancel{\mathbf{K}' \cdot \mathbf{K}'} \Rightarrow$$

$$\mathbf{P} \cdot \mathbf{K}' + \mathbf{K} \cdot \mathbf{K}' = \mathbf{P} \cdot \mathbf{K} \quad (2.4)$$

Following Longair (2011) notation, the scattering angle is given by the dot product of the position vector before and after the collision $\mathbf{i}_k \cdot \mathbf{i}_{k'} = \cos\alpha$. Setting the angle between the photon and the velocity vector of the electron θ and θ' , before and after the collision respectively, the cosines are $\cos\theta = \mathbf{i}_k \cdot \mathbf{u}/|\mathbf{u}|$ and $\cos\theta' = \mathbf{i}_{k'} \cdot \mathbf{u}'/|\mathbf{u}'|$. Hence equation (2.4) is:

$$\begin{aligned} \mathbf{P} \cdot \mathbf{K}' &= \gamma m_e h\nu' \left(1 - \frac{\mathbf{u}}{|\mathbf{u}|} \cdot \mathbf{i}_{k'} \right) \\ \mathbf{K} \cdot \mathbf{K}' &= \frac{h\nu}{c} \cdot \frac{h\nu'}{c} (1 - \cos\alpha) \\ \mathbf{P} \cdot \mathbf{K} &= \gamma m_e h\nu \left(1 - \frac{\mathbf{u}}{|\mathbf{u}|} \cdot \mathbf{i}_k \right) \\ \gamma m_e h\nu' \left(1 - \frac{\mathbf{u}}{|\mathbf{u}|} \cdot \mathbf{i}_{k'} \right) + \frac{h\nu}{c} \cdot \frac{h\nu'}{c} (1 - \cos\alpha) &= \gamma m_e h\nu \left(1 - \frac{\mathbf{u}}{|\mathbf{u}|} \cdot \mathbf{i}_k \right) \Rightarrow \\ \gamma m_e h\nu' (1 - u\cos\theta') + \frac{h\nu}{c} \cdot \frac{h\nu'}{c} (1 - \cos\alpha) &= \gamma m_e h\nu (1 - u\cos\theta) \Rightarrow \\ \frac{\nu'}{\nu} \left[\frac{\gamma m_e}{c^2} h\nu (1 - \cos\alpha) + \left(1 - \frac{u}{c} \cos\theta' \right) \right] &= \left(1 - \frac{u}{c} \cos\theta \right) \Rightarrow \\ \frac{\nu'}{\nu} &= \frac{1 - (u/c)\cos\theta}{1 - (u/c)\cos\theta' + (h\nu/\gamma m_e c^2)(1 - \cos\alpha)} \end{aligned} \quad (2.5)$$

For a stationary electron ($u = 0, \gamma = 1$):

2 Interactions of High Energy Photons

$$\frac{\nu'}{\nu} = \frac{1}{1 + (h\nu/\gamma m_e c^2)(1 - \cos\alpha)}$$

and for the wavelength:

$$\frac{\Delta\lambda}{\lambda} = \frac{\lambda' - \lambda}{\lambda} = \frac{h\nu}{m_e c^2} (1 - \cos\alpha)$$

The traditional *Compton effect* is referred to energy transfer from the photons to electrons mostly called “*recoil effect*”. In the low energy regime $h\nu \ll m_e c^2$ and $u \ll c$ the Thompson cross-section describes successfully the collisions. However, if the photons have energy $h\nu \gtrsim m_e c^2$ or the electrons move with relativistic velocities $\gamma \gg 1$, then quantum relativistic cross-section must be taken into account. The relevant total cross-section is given by the Klein-Nishina formula (eq. 9.28, Longair, 2011):

$$\sigma_{K-N} = \pi^2 r_e^2 \frac{1}{x} \left\{ \left[1 - \frac{2(x-1)}{x^2} \right] \ln(2x+1) + \frac{1}{2} + \frac{4}{x} - \frac{1}{2(2x+1)^2} \right\} \quad (2.6)$$

where $x = h\nu/m_e c^2$ and $r_e = e^2/4\pi\epsilon_0 m_e c^2$ is the classical electron radius. It is easy to show that for low energy photons ($x \ll 1$) the above formula boils down to:

$$\sigma_{K-N} = \frac{8\pi}{3} r_e^2 (1 - 2x) = \sigma_T (1 - 2x) \approx \sigma_T \quad (2.7)$$

where $\sigma_T = 8\pi r_e^2/3$ is the Thompson cross-section. On the other hand, in the ultra-relativistic limit $\gamma \gg 1$, the Klein-Nishina cross-section becomes:

Yet,

$$\sigma_{K-N} = \pi r_e^2 \frac{1}{x} \left(\ln 2x + \frac{1}{2} \right) \quad (2.8)$$

so that the cross-section declines as x^{-1} in high energies. In Figure (2.1) (Fig. 9.4 Longair, 2011) there is a schematic of the cross-section against the photon energy.

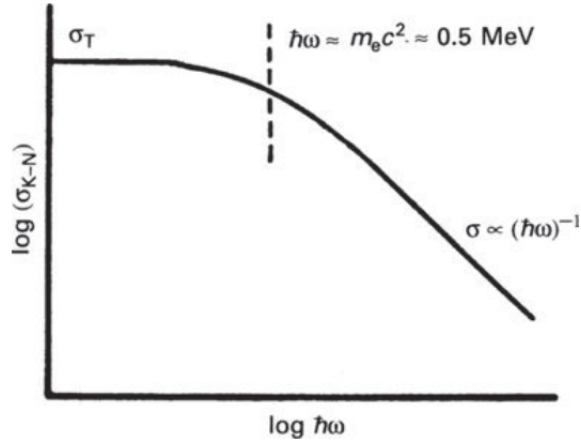


Figure 2.1: The dependence of the Klein-Nishina cross-section upon photon energy. In x-axis $h\nu = h \cdot \frac{\omega}{2\pi} = \hbar\omega$

2.2 Inverse Compton Scattering

As said before, *Compton scattering* is considered to be a recoil effect procedure where photons lose energy and electrons are being accelerated. Hence, the opposite procedure, where the photon field gains energy after colliding with very energetic electrons, is called *Inverse Compton Scattering (ICS)*. We follow Longair (2011) to illustrate the framework of that process in order to derive the net energy gain rate of the photon field.

For a photon in the laboratory frame of reference S, with energy $h\nu$ and incidence angle θ , the energy in the rest frame of the electron S', according to the Doppler shift formula is:

$$h\nu' = \gamma h\nu [1 + (u/c)\cos\theta] \quad (2.9)$$

Assuming the photon energy is much less than the rest mass energy of the electron $h\nu' \ll m_e c^2$, the energy loss in the energy loss rate of the electron in S' is:

$$-\left(\frac{dE}{dt}\right)' = \sigma_{TC} \cdot U'_{rad} \quad (2.10)$$

The energy density of photons in S is $Nh\nu$, where N is the number density. Therefore, the flux density is $U_{rad}c = Nh\nu c$. If we want to transform it to the electron rest frame S', the photon energy is given by (2.9), whereas the number density of photon scattered upon electron is greater by a factor of $\gamma[1 + (u/c)\cos\theta]$ (see par. 9.3 Longair, 2011). Hence, the energy density in S' is:

$$U'_{rad} = [\gamma(1 + (u/c)\cos\theta)]^2 U_{rad} \quad (2.11)$$

2 Interactions of High Energy Photons

assuming isotropic radiation field and by integrating over solid angle:

$$dU'_{rad} = U_{rad}\gamma^2[1 + (u/c)\cos\theta]^2 d\Omega = U_{rad}\gamma^2[1 + (u/c)\cos\theta]^2 \frac{1}{2}\sin\theta d\theta \quad (2.12)$$

$$U'_{rad} = U_{rad} \int_0^\pi \gamma^2[1 + (u/c)\cos\theta]^2 \frac{1}{2}\sin\theta d\theta = \frac{4}{3}U_{rad} \left(\gamma^2 + \frac{1}{4} \right) \quad (2.13)$$

For $(dE/dt) = (dE/dt)'$ and by substituting eq. (2.13) into eq. (2.10):

$$\frac{dE}{dt} = \frac{4}{3}\sigma_T c U_{rad} \left(\gamma^2 - \frac{1}{4} \right) \quad (2.14)$$

and if we subtract the energy loss of the photon field due to recoil effect, we have the net energy gain:

$$\frac{dE}{dt} = \frac{4}{3}\sigma_T c U_{rad} \left(\gamma^2 - \frac{1}{4} \right) - \sigma_T c U_{rad} = \frac{4}{3}\sigma_T c U_{rad}(\gamma^2 - 1) \Rightarrow$$

$$\{(\gamma^2 - 1) = (u^2/c^2)\gamma^2\} \Rightarrow$$

the net energy gain for the photons during the Inverse Compton scattering is:

$$\frac{dE}{dt} = \frac{4}{3}\sigma_T c U_{rad} \left(\frac{u^2}{c^2} \right) \gamma^2 \quad (2.15)$$

2.3 Comptonization

When Inverse Compton Scattering dominates in a medium, and other mechanisms like Bremsstrahlung, do not contribute as much, the spectrum produced is characterized by a physical process called *Comptonization*. Comptonization can be extremely important when low energy photon field is being upscattered in hot plasma, where photons gain a great amount of energy. Such environments can be found in X-Ray binaries, near the SMBH of AGN, in hot gas in galaxy clusters etc.

2.3.1 The simple physical framework

In the non-relativistic regime in which the temperature of the plasma is much lower the rest mass energy of the electrons ($kT_e \ll m_e c^2$) and photons have low energy ($h\nu \ll m_e c^2$), the Thompson cross-section σ_T can be used to illustrate the interactions between photons and electrons. In order to find the net energy exchange between the electrons and photons, the photon energy loss and the photon energy gain must be calculated.

The fractional energy loss change of a photon per collision is (eq. 9.46 Longair (2011)):

$$\frac{\Delta\varepsilon}{\varepsilon} = \frac{h\nu}{m_e c^2} (1 - \cos\alpha) \quad (2.16)$$

where α is the collision angle between the photon and the electron.

2 Interactions of High Energy Photons

Thompson scattering is symmetrical in the frame of reference of the electron, and as a result, the average value cancels out the cosine of the collision angle, and so the average energy that is being transferred from the photon to the electron is:

$$\left\langle \frac{\Delta\varepsilon}{\varepsilon} \right\rangle = \frac{h\nu}{m_e c^2} \quad (2.17)$$

this is also called *recoil effect* and describes the cooling of the photon field.

Next, the energy gain of the photons must be derived. To do so, the energy loss rate of high energy electrons due to ICS will be used and is given by eq 9.48 Longair (2011):

$$\frac{dE}{dt} = \frac{4}{3} \sigma_T c u_{rad} \beta^2 \quad (2.18)$$

where σ_T is the Thompson cross-section, c is the speed of light, u_{rad} is the energy density of the radiation and $\beta = v/c$. The number of collision per second is:

$$\frac{collisions}{time} \left[\frac{\#}{s} \right] = \sigma_T N_{phot} c = \sigma_T u_{rad} c / h\nu \quad (2.19)$$

now if we divide equations (2.18) and (2.19) we can get the average energy gain per collision:

$$\begin{aligned} \frac{dE}{dt} \times \left(\frac{collisions}{time} \left[\frac{\#}{s} \right] \right)^{-1} &= \frac{4}{3} \frac{v^2}{c^2} \times \frac{u_{rad}}{N_{phot}}; \\ \left[\frac{u_{rad}}{N_{phot}} \right] &= \frac{\frac{erg}{cm^3}}{\frac{particles(\#)}{cm^3}} = \frac{erg}{\#} \end{aligned}$$

by combining the two equations we have:

$$\left\langle \frac{\Delta\varepsilon}{\varepsilon} \right\rangle = \frac{4}{3} \left(\frac{v}{c} \right)^2 \quad (2.20)$$

which is the average energy gain per collision.

Assuming the electrons have thermal distribution and temperature T_e , the energy equilibrium is:

$$\begin{aligned} \frac{1}{2} m_e \langle v^2 \rangle &= \frac{3}{2} k T_e \Rightarrow \\ \langle v^2 \rangle &= 3kT_e/m_e \Rightarrow \\ \left\langle \frac{v^2}{c^2} \right\rangle &= \frac{3kT_e}{m_e c^2} \end{aligned} \quad (2.21)$$

and by substituting (2.21) in (2.20):

$$\frac{\Delta\varepsilon}{\varepsilon} = \frac{4kT_e}{m_e c^2} \quad (2.22)$$

2 Interactions of High Energy Photons

which is the energy that photons gain per collision when they interact with a thermal electron cloud (Longair, 2011; Titarchuk, 1994).

Hence, the net energy exchange for photons that interact with hot electrons is the energy loss (2.17) subtracted from the energy gain (2.22) and it is:

$$\frac{\Delta\varepsilon}{\varepsilon} = \frac{4kT_e - h\nu}{m_e c^2} \quad (2.23)$$

Equation (2.23) shows three different regimes; (i) when $4kT_e = h\nu$ no energy is being transferred between photons and electrons, (ii) when $4kT_e > h\nu$ energy is being transferred from the electrons to the photons and (iii) when $4kT_e < h\nu$ energy is being transferred from the photons to the electrons.

Let's focus on the regime where electrons are much hotter than the seed photon field. The energy gain is $\sim 4kT_e/m_e c^2$ and the number of collisions a photon makes before escaping can be calculated. For electron density N_e and the size of the medium l , the optical depth is:

$$\tau_e = N_e \sigma_T l \quad (2.24)$$

The *mean free path*, which is the distance a photon travels through a random walk, is $\lambda_e = (N_e \sigma_T)^{-1}$ and hence, the number of scatterings N a photon does before escaping a medium of length l is:

$$N = \left(\frac{l}{\lambda_e} \right)^2 = \tau_e^2 \quad (2.25)$$

Finally, the initial photons emerge from a medium of hot electron plasma with energy $\varepsilon_f = \varepsilon_i e^y$ (Rybicki and Lightman, 1986) where the *Comptonization Parameter* y is (eq. 9.53 Longair (2011)):

$$y = \frac{kT_e}{m_e c^2} \times \max(\tau_e, \tau_e^2) \quad (2.26)$$

where $\max(\tau_e, \tau_e^2)$ refers to the maximum value of the optical depth when the medium has $\tau_e \ll 1$ and $\tau_e \gg 1$ respectively. In order to change significantly the spectrum of the photons the y parameter must be (Titarchuk, 1994):

$$y = \frac{kT_e}{m_e c^2} \tau_e^2 \gtrsim \frac{1}{4} \quad (2.27)$$

2.3.2 Generalized Comptonization Models

The theory developed in early 80s-90s (Titarchuk, 1994; Sunyaev and Titarchuk, 1980) illustrates the spectral formation in thermal X-Ray sources, where *Comptonization* is the main mechanism that takes place and Klein-Nishina and relativistic corrections are important. Plasma physical parameters such as temperature and optical depth, along with the asymptotic escape rate of the photons determine the final shape of the hard

2 Interactions of High Energy Photons

X-ray spectrum. At high temperature, where inequality (2.27) is valid, *Comptonization* is dominant.

In order to find the shape of the emerging spectrum, the *Comptonization Radiative Transfer* problem must be solved, which is reduced to the diffusion problem over space and energy. We focus on the case when energy is being transferred from electrons to photons and the initial photon energy is much less than the electron energy, which is the regime when equation (2.22) is valid. The comptonization parameter y for a random walk trajectory with time duration t is:

$$y_{tr} = \frac{4kT_e}{m_e c^2} N_e \sigma_T c t \quad (2.28)$$

and determines the photon energy gain. For a plasma cloud with optical depth $\tau_o \gg 1$ the mean number of scatterings is $\bar{u} \sim \tau_o^2$. Hence, we can distinguish two different cases, one when photons undergo less scatterings than the mean number, and the case when the scattering number is greater than the mean number. In the first scenario ($u \ll \bar{u}$) the photons retain the initial information about the spectral, angular and spatial distribution. In the latter, the photons undergo $u \gg \bar{u}$ number of scatterings and the spectrum they form is characterized by the plasma optical depth τ_o and temperature kT_e , and is almost independent of the initial seed photon field distribution (Titarchuk, 1994). The hard X-ray component is formed by these photons and as a result the scattering procedure is different from isotropic. The diffusion coefficient ϕ_ν which is responsible for the photon direction, is obtained by averaging cosine of the angular variable θ over all directions. In the isotropic case, this equals $1/3$. However, in relativistic energies and temperatures, photons are getting harder and harder due to ICS and the differential cross section deviates from an isotropic one. As a result, a transport factor is added which is a function of the dimensionless temperature of both photons and electrons (Titarchuk, 1994). Most photons are collimated along the longest size of the medium (diameter for sphere; along the disk plane for disk). Therefore, the radiative transfer problem can be simplified assuming forward and backward scattering directions. Forward scattering does not change the energy of the photon in contrary of backward scattering which is the most energetic phenomenon. While the temperature of the photon is getting higher, forward scattering is being favored and the hard X-ray tail is formed.

The radiative transfer theory

In the optical thick case ($\tau_o \gg 1$), the transport cross section of scattering electrons is (Titarchuk, 1994):

$$\sigma_{tr} = \frac{\sigma_T}{\lambda_{tr}(x, \Theta)} = \int \left(1 - \frac{\nu}{\nu'} \cos\theta\right) d\sigma_c(\nu \rightarrow \nu') \quad (2.29)$$

where $\Theta = kT_e/m_e c^2$ is the dimensionless temperature, $x = h\nu/m_e c^2$, σ_T is the Thompson cross section, $d\sigma_c(\nu \rightarrow \nu')$ is the differential cross section of Compton scattering averaged over Maxwellian distribution (Shestakov et al., 1988). Finally, λ_{tr} is the transport coefficient for anisotropical scattering and it is given by (eq 2a, Titarchuk, 1994):

2 Interactions of High Energy Photons

$$\lambda_{tr} = [1 + 2.8(1 - 1.1\Theta)x - 0.44x^2] \quad (2.30)$$

The energy diffusion coefficient determines the time evolution of the photon energy and for plasma temperature below 100keV it is given by:

$$\eta(x, \Theta) = \frac{x^4}{1 + 4.6x + 1.1x^2} \left[1 + \frac{f_o(\Theta)}{1 + 10.2x} \right] \quad (2.31)$$

where $f_o(\Theta) = 2.5\Theta + 1.875\Theta^2(1 - \Theta)$.

The solution of the diffusion problem can be reduced to the solution of a differential equation that illustrates the diffusion of the photons in both the energy and configuration space. In equation (2.32), the first term is the energy space diffusion operator, which is the operator that describes the energy gain and recoil effect of the photons, and the second term is related to the spatial diffusion. We define the dimensionless variables $x = h\nu/mc^2$, $\tau = \tau_T$ is the Thompson optical coordinate (see Appendix A, Titarchuk, 1994); the photon occupation number $n(x, \tau) = I_\nu c^2/2\nu^3$ and $B_o(x, \tau)$ is the primary source distribution. Hence, the differential equation that describes the radiative transfer problem is:

$$L_\nu n + L_\tau^{(d)} n = -\frac{B_o(x, \tau)\lambda_{tr}^{-1}(x\Theta)}{x^3} \quad (2.32)$$

λ_{tr} is the transport coefficient for anisotropical scattering and it is given by (eq 2a, Titarchuk, 1994):

$$\lambda_{tr} = [1 + 2.8(1 - 1.1\Theta)x - 0.44x^2] \quad (2.33)$$

The energy diffusion operator is:

$$L_\nu = \frac{\Theta\lambda_{tr}^{-1}(x\Theta)}{x^2} \frac{\partial}{\partial x} \left[\eta(x\Theta, \Theta) \left(\frac{\partial}{\partial x} + E \right) \right] \quad (2.34)$$

where E is the identity operator, and the spatial diffusion operator is:

$$L_\tau^{(d)} = \begin{cases} \frac{1}{3} \frac{1}{\tau^2} \frac{\partial}{\partial \tau} \tau^2 \frac{\partial}{\partial \tau} & \text{spherical geometry} \\ \frac{1}{3} \frac{d^2}{d\tau^2} & \text{plane/disk geometry} \end{cases} \quad (2.35)$$

The right-hand side term of equation (2.32) is factorable and can be written as product of two functions of x and τ as:

$$\frac{B_o(x, \tau)\lambda_{tr}^{-1}(x\Theta)}{x^3} = \psi(x)r(\tau) \quad (2.36)$$

and therefore the solution of (2.32) is the convolution (Appendix A, Titarchuk, 1994):

$$n(x, \tau) = \int_0^\infty N(x, u)R(\tau, u)du \quad (2.37)$$

2 Interactions of High Energy Photons

where u is a dimensionless variable of time related to the number of scatterings a photon does before escaping.

$N(x, u)$ is the time-dependent solution in energy space:

$$\frac{\partial N}{\partial u} = L_\nu N \quad (2.38)$$

with initial condition $N(x, 0) = \psi(x)$.

The second term $R(\tau, u)$ is the time-dependent solution for the spatial diffusion:

$$\frac{\partial R}{\partial u} = L_\tau^{(d)} R \quad (2.39)$$

with initial condition $R(\tau, 0) = r(\tau)$.

In the case of Compton upscattering $r(\tau)$ is the first eigenfunction of the space operator $L_\tau^{(d)}$ (Titarchuk, 1994) and hence, the solution of (2.39) along with the initial condition, can be written:

$$R(\tau, u) = R_1(\tau)e^{-\beta u} \quad (2.40)$$

Therefore, the solution of $n(x, \tau)$ is:

$$n(x, \tau) = n_1(x, \tau) = R_1(\tau) \int_0^\infty N(x, u)e^{-\beta u} du = R_1(\tau)N_1(x) \quad (2.41)$$

The Comptonization problem reduces to solving the *Comptonization Stationary Equation (CSE)* for $N_1(x)$ (eq. 15, Titarchuk, 1994):

$$L_\nu N_1 - \beta N_1 = -\psi(x) \quad (2.42)$$

The meaning of equation (2.41) is that the process of energy gain and random walk through the plasma are independent of each other. The solution $N_1(x)$ determines the shape of the emergent spectrum. This means that for an isothermal plasma disk/sphere, the shape of the hard radiation spectrum does not depend on the low frequency seed photons and therefore this physical framework is suitable to study the intrinsic properties of the corona unbiased by the input photon field.

The second term of equation (2.42), which is related to the escape rate of the photons, is proportional to the occupation number N_I with the coefficient β . The time-dependent function $R(\tau, u)$ determines the distribution of photons over the dimensionless time u they spend inside the medium. The probability a photon undergoes u scatterings $u \gg \bar{u}$ is given by the asymptotic relation (eq. 17, Titarchuk, 1994):

$$P_{as}(u) = A(\bar{u}, \tau)e^{-\beta u} \quad (2.43)$$

where $A(\bar{u}, \tau)$ is a normalization constant. This relation implies that the fractional number of photons which random walk out of the plasma cloud becomes $e^{-\beta}$ less with each collision. The parameter β is given by the relation $\beta = \lambda_1^2/3$ where λ_1 is the first

2 Interactions of High Energy Photons

eigenvalue of the spatial diffusion operator $L_\tau^{(d)}$ for the disk and spherical geometry (eq. (2.35)). The parameter β has been calculated by Titarchuk (1994) and has been derived both analytically and numerically, and Figure 2.2 shows the relation between β and the optical depth τ_o . The expressions derived are:

- analytical

$$\beta = \begin{cases} \ln \left[\frac{2}{3\tau_o \ln(1/2\tau_o)} \right] & \text{disk} \\ \ln \frac{4}{3\tau_o} & \text{sphere} \end{cases} \quad (2.44)$$

- numerical

$$\beta = \begin{cases} \frac{\pi^2}{12(\tau_o+2/3)^2} (1 - e^{-1.35\tau_o}) + 0.45e^{-3.7\tau_o} \ln \frac{10}{3\tau_o} & \text{disk} \\ \frac{\pi^2}{12(\tau_o+2/3)^2} (1 - e^{-0.7\tau_o}) + e^{-1.4\tau_o} \ln \frac{4}{3\tau_o} & \text{sphere} \end{cases} \quad (2.45)$$

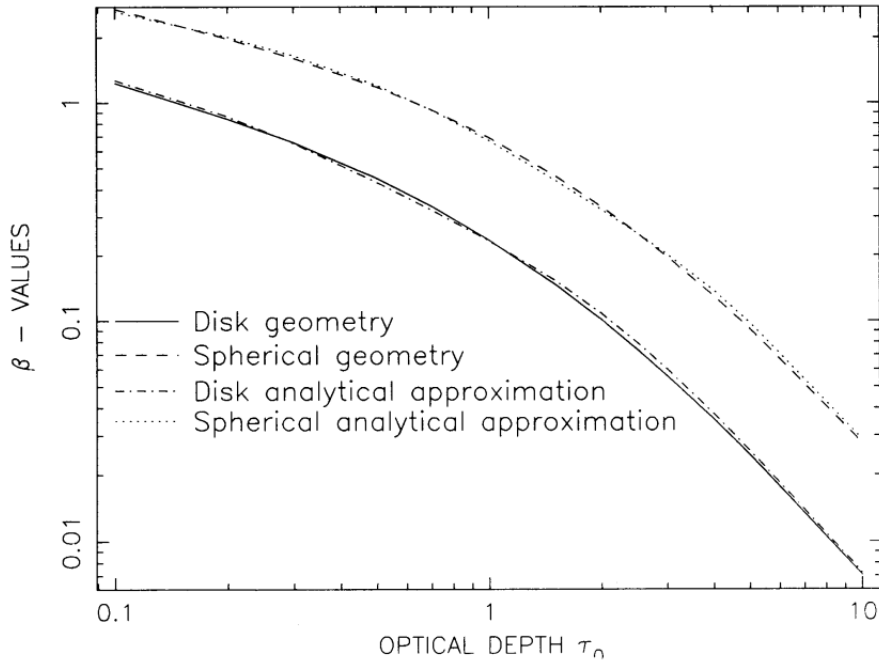


Figure 2.2: β as a function of the optical depth τ_o for the spherical and disk geometry. Both the analytical and numerical expressions are presented (Fig.1 Titarchuk, 1994).

Finally the emission spectrum can be derived by solving the homogeneous Comptonization Stationary Equation (CSE) which is given by Eq. 29 Titarchuk (1994):

2 Interactions of High Energy Photons

$$x^2 N_1'' + x[x(1 + \epsilon) + 4]N_1' + (x^2 \epsilon + 4x - \gamma)N_1 = 0 \quad (2.46)$$

where N_1 is the occupation number, $x = \mu'/\mu$ and $\mu = \eta(x\Theta, \Theta)/z^4$.

A computational interpretation of the above theoretical framework can be found in the X-ray analysis software XSPEC¹(Arnaud, 1996). The model is called *compTT*² and it is an analytical model that describes the comptonization of soft photons in hot plasma. The model works for thick and thin plasma (see Fig. 7 Hua and Titarchuk, 1995). There are 5 parameters as an input which are: (i) The redshift z ; (ii) the soft photon temperature (keV); (iii) the plasma temperature; (iv) the plasma cloud optical depth; and (v) geometry switch parameter. Redshift and geometry parameter stay frozen during the fitting process. In Figure (2.3) there are two examples of the *compTT* model for different plasma temperature and optical depth.

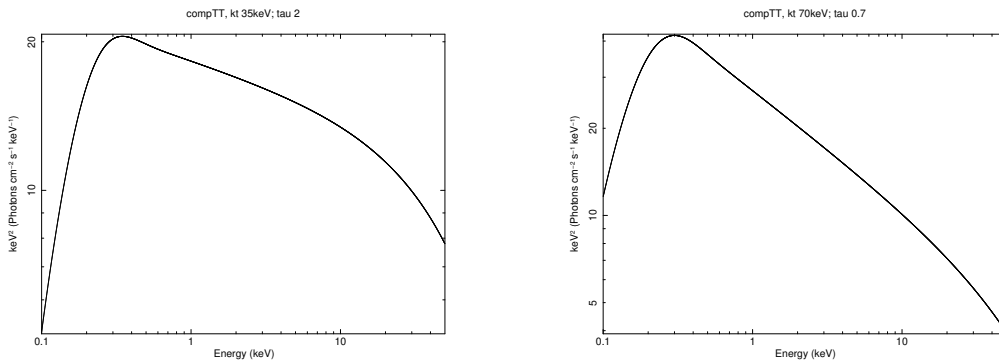


Figure 2.3: The theoretical model *compTT* for two different pairs of plasma temperature kt and optical depth τ .

¹<https://heasarc.gsfc.nasa.gov/xanadu/xspec/>

²<https://heasarc.gsfc.nasa.gov/xanadu/xspec/manual/node157.html>

3 Analysis

3.1 Introduction

Accreting Supermassive Black Holes (SMBH) are known to produce radiation in the X-ray band. Soft photons, coming from the accretion disk, are being Comptonized by hot thermal electrons around the supermassive black hole, known as the corona (e.g. Haardt and Maraschi, 1993). Compton upscattering of UV and optical photons from the inner accretion disk by coronal electrons produce a power-law-like X-ray continuum, with a cutoff at energies determined by the electron temperature T_e (Blumenthal and Gould (1970); Rybicki and Lightman (1986); Longair (2011)). Reverberation mapping of prominent emission lines and gravitation microlensing analysis have shown that the corona is relatively small and has radius $R_c < 10R_g$, where $R_g = GM_{BH}/c^2$ (e.g. Fabian et al. (2009); Chartas et al. (2009)).

X-ray spectroscopy, and in particular the study of the primary X-ray emission produced in the Comptonizing plasma, can provide important insights on the physical parameters of the corona, such as its temperature (kT_e) and optical depth (τ). The plasma temperature is related to the energy cutoff (E_c) of the hard X-ray spectrum and therefore, it requires good-quality data above 10 keV in order to study the physical parameters of the coronae and seek potential correlation with intrinsic properties of the AGN such as black hole mass (M_{BH}), luminosity (L) and Eddington ratio ($\lambda_{EDD} = L/L_{EDD}$). Hard X-ray telescopes, like *BeppoSAX*, *INTEGRAL*, *Swift/BAT* (Dadina (2007); de Rosa et al. (2012); Ricci et al. (2018)), have performed observations that have been used to study the coronae of the AGN finding that the energy cutoff (E_c) varies from 50 to 300 keV approximately.

Correlation between the physical parameters (plasma temperature, optical depth) and SMBH properties has been a matter of debate and previous studies have shown different results (e.g. Tortosa et al. (2018); Ricci et al. (2018)). In this work we study sources using observations of the *Nuclear Spectroscopic Telescope Array (NuSTAR)*, Harrison et al. 2013) and try to find out whether the corona and the SMBH affect each other. For that purpose non-jetted and unobscured AGN have been selected from the *Swift/BAT 70-month survey*. In section (3.2) we provide details about our sample along with the model that we used and then in section (3.4) the results of our analysis are presented.

3.2 The sample

3.2.1 Sample

Our sample consists of 67 AGN identified in the Swift/BAT 70 month hard X-ray catalog (Gehrels et al., 2004; Baumgartner et al., 2013). From the full catalog, we selected

sources that have a *NuSTAR* observation counterpart. Moreover, our final sample include AGN (i) with known redshifts (ii) classified as Sy1 from optical hydrogen emission line measurements (iii) the SMBH mass was available. In Figure (3.1a) the redshift of the sources is presented and ($z < 0.2$), with median of $z_m = 0.043$.

As part of its Extragalactic Legacy Surveys program, the *NuSTAR* observatory has performed snapshot ~ 20 ks observations of local AGNs detected in the all-sky survey with the Burst Alert Telescope (BAT). *NuSTAR* is a space telescope launched in 2012 and operates in the 3-79 keV band. It has two coaligned X-ray optics which focus X-ray photons onto two independent shielded focal plane modules, namely FPMA and FPMB and thanks to its focusing optics, it has a broad and high quality spectral coverage. Such high quality spectra in hard X-rays are necessary in order to constrain the high energy cutoff and therefore derive solid results for the physical parameters of the coronae. BAT spectra have not been included in our analysis due to the variability that many sources have. In other words, *NuSTAR* observations are contemporary observations, while *Swift/BAT* operates for more than a decade and the observation date of a source from *NuSTAR* and *Swift/BAT* may vary for several years, and hence the quality of the output spectra would have been affected by this selection. Furthermore, BAT spectra lack of quality (photon number) in respect to *NuSTAR* data.

3.2.2 Black hole mass

The 67 sources studied, have their black hole mass in the BAT AGN Spectroscopic Survey (BASS¹)(Koss et al., 2017; Ricci et al., 2017). In BASS catalog the mass has been derived using 4 different methods. (i) Using velocity dispersion - black hole mass relation proposed by Kormendy and Ho (2013); (ii) Using single epoch spectra of broad $H\beta$ emission lines (Trakhtenbrot and Netzer, 2012); (iii) Using single epoch spectra of broad $H\alpha$ emission lines (Greene and Ho, 2005); (iv) Using reverberation mapping for all available emission lines according to Bentz and Katz (2015) and AGN Mass catalog². The masses calculated, have been flagged for their quality with “1” for excellent and “2” for acceptable. Sources with flag number greater than “2” had issues in measuring and therefore, we have selected only “1” and “2” black hole mass measurements. In Figure (3.1b) the histogram of the sources masses illustrates that our sample contain a wide range of SMBH masses with median value $M_m = 7.88$ (\log^{M_{BH}/M_\odot}).

¹<https://www.bass-survey.com/>

²<http://www.astro.gsu.edu/AGNmass/>

3 Analysis

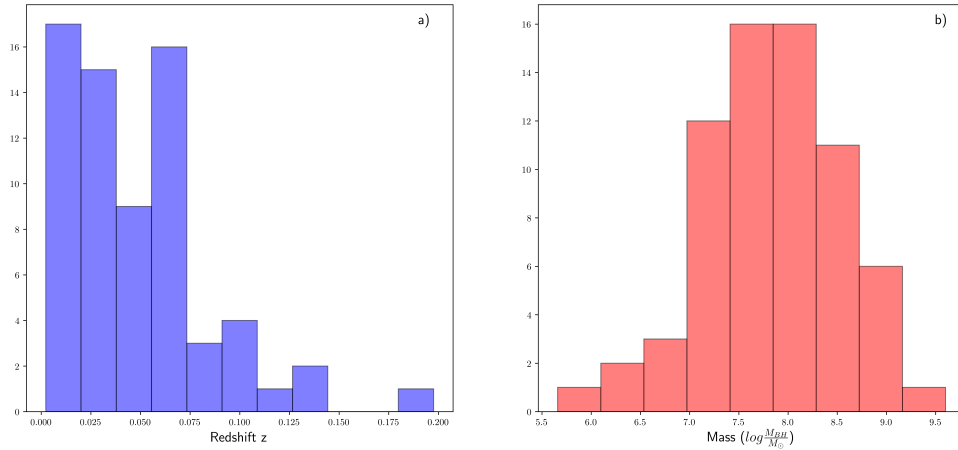


Figure 3.1: Histogram of the Redshift (left) and Black hole mass (right) for the 67 sources studied.

3.3 Spectral modeling

In order to extract the necessary parameters, Heasarc’s software for X-ray spectral fitting *XSPEC*³ (Arnaud, 1996) has been used. For the fitting purpose, the following four models available in *XSPEC* have been implemented as *WA*COMPTT+GA+PEX*: (i) *Wabs* (WA): A photo-electric absorption using Wisconsin (Morrison and McCammon, 1983) effective absorption cross section per hydrogen atom calculated as a function of energy in the 0.03-10 keV range using the most recent atomic cross section and cosmic abundance data. *Wabs* has one free parameter, the column density for hydrogen atoms N_H [$\#atoms \times 10^{22} \times cm^{-2}$]. (ii) *ComptTT*: Comptonization model that describes the reprocessed low energy radiation field being upscattered in a hot corona above the accretion disk. Through *comptTT* model the plasma temperature and optical depth have been derived and it is based on the analysis of Titarchuk (1994). It has five input parameters which are: the redshift z (fixed); the input soft photon field energy in keV; the plasma temperature in keV; the plasma optical depth; A geometry value⁴ that was set 2 (spherical geometry). (iii) Gaussian emission line (GA): A simple gaussian line profile⁵ which has two parameters. The energy of the line in keV E_{line} (free) and the line width σ set equal to 0.1. (iv) Reflection component PEXRAV (PEX): Exponentially cut off power law spectrum reflected from neutral material (Magdziarz and Zdziarski, 1995). The output spectrum is the sum of the cut-off power law and the reflection component. By setting the reflection scaling factor $rel_{refl} < 0$, the model returns the reflection com-

³<https://heasarc.gsfc.nasa.gov/xanadu/xspec/>

⁴For details see: <https://heasarc.gsfc.nasa.gov/xanadu/xspec/manual/node157.html>

⁵<https://heasarc.gsfc.nasa.gov/xanadu/xspec/manual/node175.html>

3 Analysis

ponent alone. PEXRAV's parameters are, the photon index Γ (set 1.8 fixed); the Energy cutoff ($E_c = 3 \times kt$) which was set in agreement with the plasmal temperature derived from the *compTT* model; the reflection scaling factor which was fixed -1 (fixed); the redshift z (fixed); the abundances of elements heavier than He and abundance of iron (both fixed 1); and the cosine of the inclination angle.

Having completed the fitting process, we parsed the plasma temperature, the optical depth and the soft X-ray luminosity (2-10keV). Along with the black hole mass, the Eddington ratio has been calculated using eq. (3.1).

$$\lambda_{EDD} = \frac{L_{bol}}{L_{EDD}} \quad (3.1)$$

where L_{bol} is the bolometric luminosity and it is calculated as $L_{bol} = \kappa_{2-10} \times L_{2-10}$ with $\kappa_{2-10} = 20$ being the bolometric correction (Vasudevan and Fabian, 2009). L_{EDD} is the Eddington luminosity which is given by:

$$L_{EDD} = \frac{4\pi GMm_p c}{\sigma_T} \quad (3.2)$$

3.4 Results

Figure (3.2) shows a histogram of the plasma temperature and optical depth for our sample. The filled area represents the sources of which the plasma temperature has been calculated and constrained fully, on the contrary step line is for the lower limit sources. The median of the parameters derives from the fitting described above, are presented in Table 3.1. The sample has been separated into two groups, the sources of which the plasma temperature has been constrained and the lower limit sources; sources that a lower limit of the plasma temperature has been adequately calculated. The correlation between the intrinsic properties of the plasma cloud that forms the corona of an AGN, plasma temperature and optical depth, and properties of the source as a whole, like the SMBH mass, the soft X-ray radiation and the Eddington ratio, has been on debate with no finite answer yet (e.g. Ricci et al. (2018); Kamraj et al. (2018); Tortosa et al. (2018)). In Appendix a Table containing the whole sample can be found.

Table 3.1: Table of the median values of the quantities derived from the fitting process

Source	Mass $\log(M_{BH}/M_\odot)$	kt keV	τ	L_{2-10} $\times 10^{44} \text{ erg/s}$	λ_{EDD}
Well constrained	7.91	26.45(± 0.52)	3.54(± 0.06)	0.27	0.07
Lower limit	7.78	44.75(± 1.56)	3.10(± 0.13)	0.48	0.1

3 Analysis

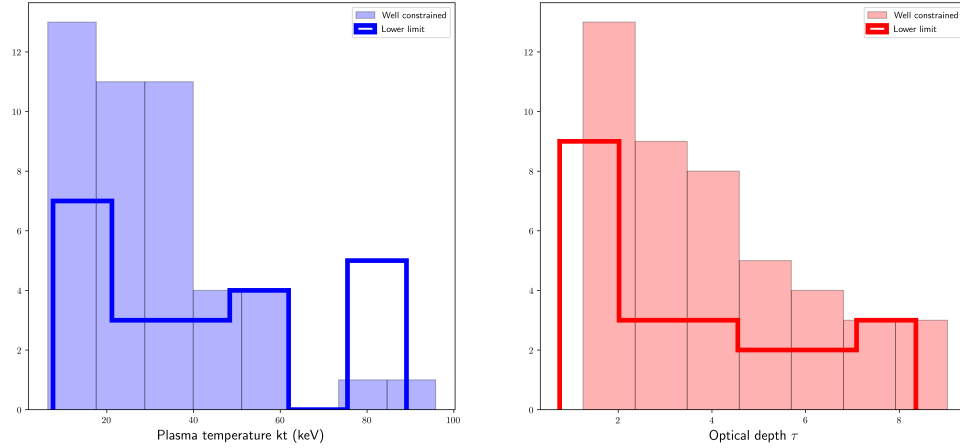


Figure 3.2: Histogram of the plasma temperature (left) and the optical depth (right). The filled area represents the sources with well constrained plasma temperature, whereas the step line represents the lower limit sources.

In figure (3.3) the sample in the plasma temperature - optical depth ($kt - \tau$) plane is depicted. A strong anticorrelation trend is present with spearman coefficient $\rho_o = -0.96$. The strong anticorrelation is expected from the physical model (comptonization) that has been used and therefore it is a good visual criterion to examine the quality of the fitting process. The fitting quality and the whether the results are physically reasonable can be tested by drawing the photon index line in the $kt - tau$ space based on the relation (Petrucci et al., 2001):

$$\Gamma = \sqrt{\frac{9}{4} + \frac{511}{\tau \cdot kt(1 + \tau/3)}} - \frac{1}{2} \quad (3.3)$$

In figures (3.4) - (3.6) the correlation of the two main physical properties of the corona (kt, τ) and three different properties ($M_{BH}, L_{2-10}, \lambda_{EDD}$) of the active nucleus are presented. In all three figures the sources have been separated into two groups as described above in order to see whether there is correlation related to each subsample. Regardless doing that, there is no clear correlation between the parameters, i.e. there are sources with certain mass value that have either hot or cold coronae and likewise high and low optical depth. In general, all the sources tend to have optical depth $\tau > 1$ and only when the plasma temperature is extremely high, significantly thin plasma clouds are present.

3 Analysis

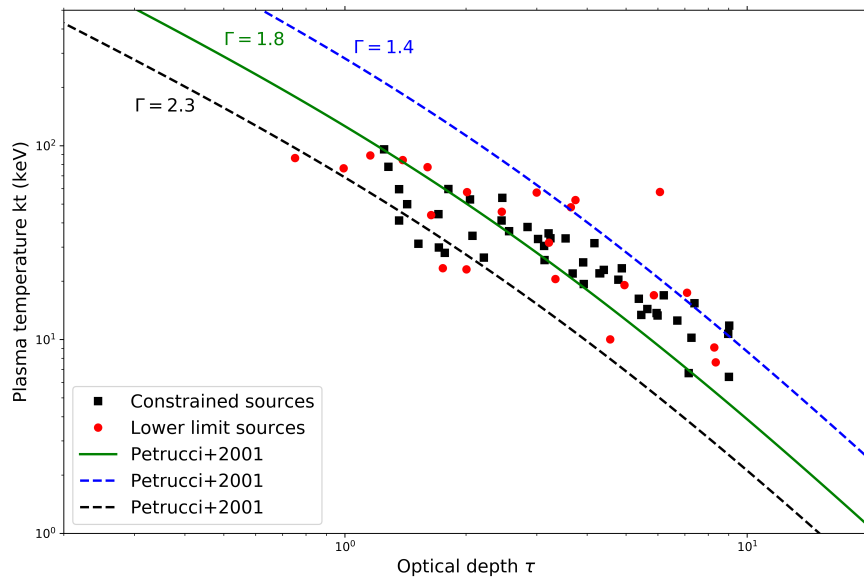


Figure 3.3: The optical depth of the corona and the plasma temperature. The black squares represent the sources of which temperature has been constrained, whereas red circles depict lower limit sources.

3 Analysis

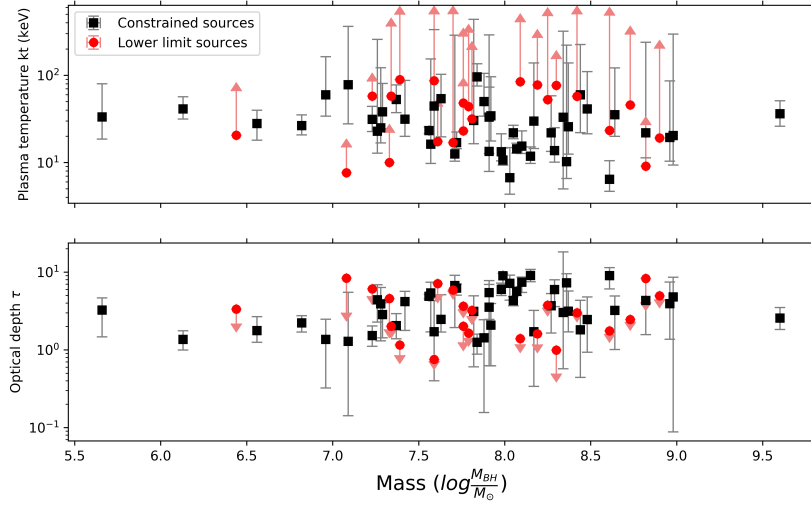


Figure 3.4: Plasma temperature and Optical depth vs the normalized SMBH mass. Black squares and red circles represent well constrained sources and lower limit sources respectively.

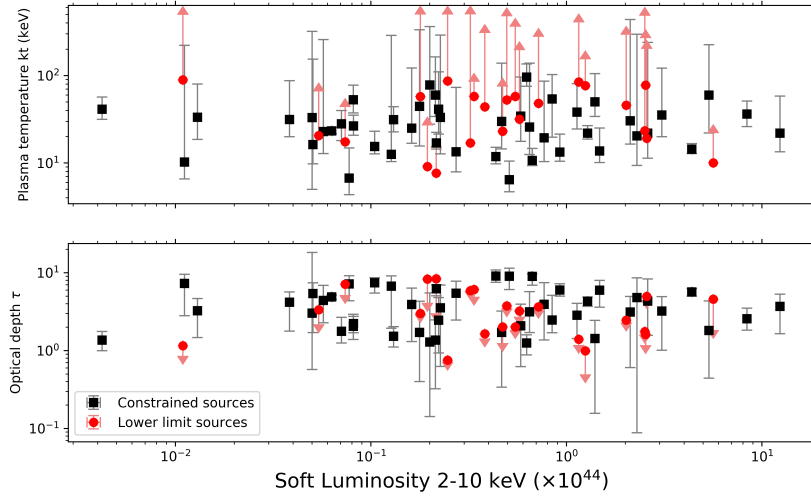


Figure 3.5: Plasma temperature and Optical depth vs the soft luminosity 2-10 keV. Black squares and red circles represent well constrained sources and lower limit sources respectively.

3 Analysis

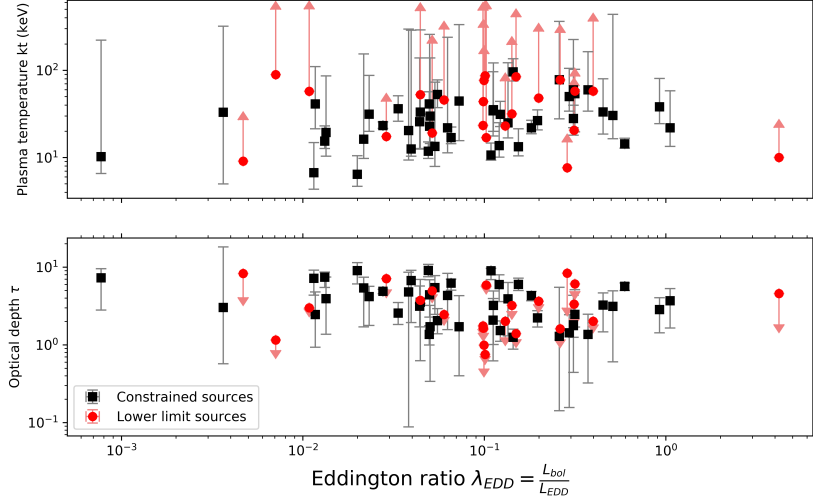


Figure 3.6: Plasma temperature and Optical depth vs the Eddington ratio λ_{EDD} . Black squares and red circles represent well constrained sources and lower limit sources respectively.

In order to understand the results, we will approach them from three different aspects. At first, a physical explanation for the non-correlation will be proposed; next, the initial assumptions of our analysis will be taken into consideration and finally we will discuss the observational limits that may have occurred and thus coronal properties seem to be independent of the SMBH.

Svensson (1984) derived an analytical form of the pair production line in the $\Theta - l$ plane where Θ is the dimensionless temperature ($\Theta = kt/mc^2$) and l is the compactness. The analytical expression is:

$$l \sim 10\Theta^{5/2}e^{1/\Theta} \quad (3.4)$$

Pair production can be initiated by photon-photon collisions in high temperatures and may be a dominant physical process in very hot coronae. If an X-ray source moves into the top right region of the parameter space (by an increase in its temperature or compactness) as seen in Figure (3.7, solid line), then it starts forming pairs rapidly, which increases the number of particles sharing the available energy, causing the energy per particle (i.e., the temperature) to drop. Hence, the pair production appears to correspond to a physical boundary/thermostat. Sources are expected to typically lie below the pair production region line.

To test this hypothesis we calculated the dimensionless temperature Θ , as well as the compactness l using the relation:

$$l = 4\pi \frac{\lambda_{EDD}}{\kappa_X} \frac{m_p R_g}{m_e R_x} \quad (3.5)$$

3 Analysis

where m_p, m_e are the proton and electron mass respectively; λ_{EDD} is the Eddington ratio that has been calculated already and R_g is the gravitational radius. We set $R_x = 10R_g$ and $\kappa_X = 3.87$ which corresponds to $\kappa_{2-10} = 20$ (Ricci et al., 2018). In Figure (3.7) our sample in the $\Theta - l$ plane is presented, with most of the sources lie below the pair production line. However, there are two scenarios that should be discussed. Whether the sources reach the hot and compact pair production region (top-right) and then cool down or there are no sources in that region at all. Despite the compactness, which is related to the eddington ratio, being in the pair production region means having plasma temperatures above 100keV. Energy cutoff analysis of Seyfert I galaxies using *BeppoSAX* and *INTEGRAL* have shown that E_c does not exceed 300keV (Dadina, 2007, 2008; Malizia et al., 2014) which is equivalent to plasma temperature $kt < 150keV$ and therefore it is quite unlikely sources reside inside the pair production region. Nevertheless, non-thermal physical (Fabian et al., 2017) states may allow sources to move into the pair region temporarily and the cool down and fall back behind the edge line.

Another part of the $\Theta - l$ plane that lacks of great number of sources is the bottom-left side which could be resided by less luminous AGN with cool coronae ($<10-15keV$). *NuSTAR* has observed luminous sources and therefore our sample does not contain low luminosity sources. Sources with low luminosity and low plasma temperature are hard to be constrained because of observational difficulties. They lie in the limit of soft X-ray telescopes like *XMM-Newton* and *Swift/XRT* while they have not been observed with *NuSTAR* yet, with future 50 or 100ks observations may fill that region. As a result, a physical explanation of the physical state of low luminosity and cool sources is still on debate.

3 Analysis

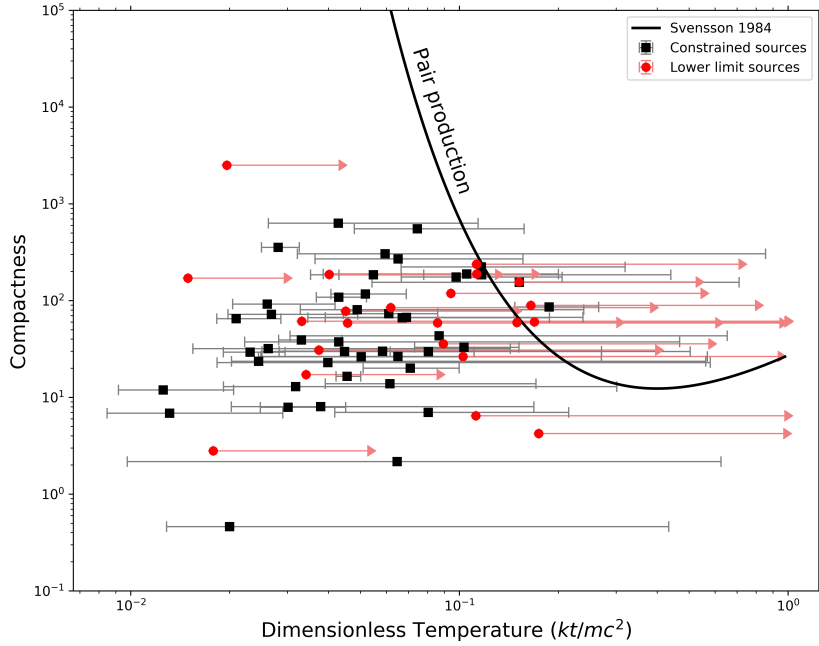


Figure 3.7: The $\Theta - l$ plane for Sy I galaxies. The *solid line* represents the analytical form of the pair production eq. (3.4). *Black squares* are sources that have their temperature constrained. *Red circles* are the sources with lower limit temperatures. The region top right (high compactness, high temperature) is dominated by pair production. The majority of our sources lie below the pair line.

3.5 Conclusion

The current work has been focused on studying non-jetted Seyfert I galaxies from the *Swift/BAT 70 month hard X-ray catalog* (Gehrels et al., 2004; Baumgartner et al., 2013) using 20ks observations of the *NuSTAR* telescope. Having parsed information from the BAT AGN Spectroscopic Survey (BASS) (Koss et al., 2017; Ricci et al., 2017), we performed spectral fitting using a comptonization model (compTT) based on Titarchuk (1994) along with some other components to improve the fitting process as described in 3.3. 67 sources have been studied with 45 sources have their plasma temperature constrained and 22 of them being lower limit sources. First, we tested the quality of the fitting by checking the photon index lines in the $kt - \tau$ plane using relation 3.3. Next, we presented the plasma temperature and optical depth versus the black hole mass, the soft luminosity and the eddington ratio and finally, a physical explanation of the results was presented. To sum up,

3 Analysis

- Comptonization as a physical process seems to model accurately the hot environment above the SMBH, as a hot plasma cloud/corona, where low energy photons coming from the disk are being upscattered and produce a hard X-ray tail, with energy cutoff two or three times the plasma temperature depending on the optical depth. Our sources are placed around the theoretical line that represents photon index of 1.8, as a result we can confirm that Seyfert I galaxies host a hot corona that comptonizes low energy photons and produce spectrum with photon index around 1.8 along with a high energy cutoff.
- No correlation has been found between the physical properties of the corona, i.e. the plasma temperature (kT) and the optical depth (τ), and intrinsic properties of the SMBH. We looked for potential correlation with the SMBH mass, the soft luminosity 2-10keV, and the Eddington ratio (λ_{EDD}). In none of the cases tested any significant correlation found and therefore, the two regions appear to evolve independently.
- A physical mechanism that has been proposed to be capable of regulating the conditions in the coronae of AGN is pair production. The pair production process can be ignited when sources reach a specific region in the $\Theta - l$ plane determined by an analytical expression (Svensson, 1984). The sources studied lie below this line which indicates that the pair production may actually be a physical thermostat that works on such plasma clouds.
- Studies with high energy telescopes have shown that it is unlikely sources in thermal state reside in the pair production region, however our analysis does not let us provide solid conclusions on that hypothesis. Moreover, low luminosity sources with cool coronae are also in question due to lack of observations of these objects. Future observations will help us investigate these sources and study their properties and try to find out whether there is a connection between coronae and the SMBH in these sources.

Active Galaxies and their nuclei are among the most exotic celestial objects. The light from these sources can be examined either for variability or spectroscopically in order to understand the physics that drives phenomena in such objects. The high energy part of the spectrum help us dig into the innermost part of AGN and study the accretion disk and the corona above it. Modern high energy telescopes like *NuSTAR* provide us excellent data in order to constrain the physical parameters according to theoretical models. Correlation between the corona and the disk, along with the heating mechanism of the corona are still on debate. Further observations may reveal some of the secrets that are hidden in AGN, and eventually learn more about the universe.

4 Appendix

Table 4.1: The sample sources with plasma temperature constrained

Name	Obs ID	Mass	kt	τ	L_{2-10}	λ_{EDD}	χ^2/dof
		$\log(M_{BH}/M_{\odot})$	keV		$\times 10^{44} \text{ erg/s}$		
Mkn335	60001041005	7.23	$31.18^{+12.74}_{-8.52}$	$1.52^{+0.51}_{-0.42}$	0.13	0.12	1.08
IC4329A	60001045002	7.84	$95.80^{+39.83}_{-20.48}$	$1.25^{+0.34}_{-0.37}$	0.63	0.14	1.22
Mrk766	60001048002	6.82	$26.45^{+8.78}_{-5.67}$	$2.22^{+0.54}_{-0.52}$	0.08	0.20	1.12
NGC4051	60001050008	6.13	$41.11^{+15.53}_{-9.63}$	$1.36^{+0.40}_{-0.37}$	0.00	0.05	1.02
4C74d26	60001080006	9.6	$36.21^{+14.85}_{-10.17}$	$2.56^{+0.94}_{-0.73}$	8.39	0.03	1.01
3C390.3	60001082003	8.64	$35.27^{+86.26}_{-15.30}$	$3.21^{+1.73}_{-2.20}$	3.08	0.11	1.06
NGC4151	60001111005	7.56	$23.28^{+2.33}_{-1.74}$	$4.88^{+0.28}_{-0.33}$	0.06	0.03	1.32
NGC5548	60002044008	7.72	$16.90^{+5.52}_{-2.49}$	$6.20^{+0.80}_{-1.15}$	0.22	0.07	0.98
NGC0985	60061025002	7.92	$34.25^{+61.76}_{-16.58}$	$2.08^{+1.87}_{-1.45}$	0.58	0.11	1.05
SWIFTJ0845d0m3531	60061085002	8.98	$20.35^{+275.86}_{-10.99}$	$4.79^{+3.82}_{-4.70}$	2.30	0.04	0.96
Mrk704	60061090002	8.48	$41.10^{+68.82}_{-19.75}$	$2.45^{+2.33}_{-1.52}$	0.22	0.01	1.07
2MASXJ15144217m8123377	60061263002	8.96	$19.33^{+66.76}_{-8.99}$	$3.93^{+3.53}_{-2.56}$	0.77	0.01	0.84
Mrk290	60061266002	7.28	$24.99^{+97.12}_{-8.23}$	$3.91^{+2.42}_{-2.61}$	0.16	0.14	0.96
IGRJ21247p5058	60061305002	7.63	$53.80^{+48.48}_{-34.11}$	$2.46^{+2.66}_{-0.77}$	0.85	0.32	1.01
Mrk728	60061338002	7.71	$12.52^{+274.52}_{-2.17}$	$6.70^{+2.40}_{-4.77}$	0.13	0.04	1.08
2MASXJ21192912p3332566	60061358002	8.37	$25.68^{+112.54}_{-13.17}$	$3.13^{+2.56}_{-1.43}$	0.65	0.04	0.95
NGC7469	60101001002	6.96	$59.59^{+103.67}_{-25.62}$	$1.36^{+1.11}_{-1.04}$	0.21	0.37	0.99
IGRJ19378m0617	60101003002	6.56	$27.99^{+11.80}_{-9.99}$	$1.77^{+0.90}_{-0.52}$	0.07	0.31	1.02
1H ₀ 419m577	60101039002	8.07	$14.36^{+2.30}_{-1.58}$	$5.65^{+0.59}_{-0.64}$	4.38	0.59	1.03
Mrk509	60101043002	8.05	$21.95^{+4.72}_{-3.19}$	$4.29^{+0.56}_{-0.61}$	1.28	0.18	1.08
NGC3783	60101110004	7.37	$52.78^{+24.78}_{-15.44}$	$2.05^{+0.88}_{-0.66}$	0.08	0.06	1.07
MR2251m178	60102025008	8.44	$59.75^{+165.06}_{-37.78}$	$1.81^{+2.53}_{-1.37}$	5.37	0.31	0.95
Mrk6	60102044004	8.1	$15.40^{+7.64}_{-2.72}$	$7.40^{+1.23}_{-1.92}$	0.10	0.01	0.96
Mrk1148	60160028002	7.82	$30.37^{+406.47}_{-13.94}$	$3.13^{+1.83}_{-2.52}$	2.12	0.51	1.03
Mrk1018	60160087002	8.03	$6.71^{+8.13}_{-2.38}$	$7.16^{+1.99}_{-2.81}$	0.08	0.01	0.98
Mrk376	60160288002	8.17	$29.84^{+108.57}_{-15.39}$	$1.71^{+1.50}_{-1.37}$	0.47	0.05	1.00
3C206	60160332002	8.27	$21.89^{+36.40}_{-8.48}$	$3.68^{+1.62}_{-2.04}$	12.37	1.06	0.99
SDSSJ104326d47p110524d2	60160406002	7.91	$33.21^{+257.12}_{-20.50}$	$3.54^{+3.39}_{-2.91}$	0.23	0.04	1.06
SBS1136p594	60160443002	7.98	$13.30^{+8.10}_{-2.86}$	$5.99^{+1.22}_{-1.00}$	0.93	0.15	0.97
UM614	60160560002	7.09	$77.80^{+284.82}_{-50.10}$	$1.28^{+4.22}_{-1.14}$	0.20	0.26	0.98
Mrk1392	60160605002	7.59	$44.33^{+289.53}_{-28.72}$	$1.71^{+2.59}_{-1.31}$	0.18	0.07	1.16
WKK6092	60160632002	7.26	$22.86^{+234.54}_{-10.05}$	$4.40^{+2.46}_{-2.13}$	0.06	0.05	1.11
1RXSJ174538d1p290823	60160674002	8.82	$21.94^{+217.10}_{-10.59}$	$4.31^{+3.98}_{-2.74}$	2.61	0.06	1.16
2MASXJ18560128p1538059	60160701002	8.29	$13.69^{+11.36}_{-3.59}$	$5.96^{+2.02}_{-2.35}$	1.48	0.12	1.02

4 Appendix

Table 4.2: Continue of Table 4.1

Name	Obs ID	Mass	kt	τ	L_{2-10}	λ_{EDD}	χ^2/dof
		$\log(M_{BH}/M_{\odot})$	keV		$\times 10^{44} \text{ erg/s}$		
2MASSJ19334715p3254259	60160714002	7.88	49.93 ^{+55.03} _{-15.93}	1.43 ^{+1.01} _{-1.27}	1.40	0.29	1.04
3C445	60160788002	7.99	10.70 ^{+3.93} _{-1.36}	8.98 ^{+0.63} _{-2.09}	0.67	0.11	1.01
Mrk110	60201025002	7.29	38.07 ^{+42.38} _{-13.60}	2.85 ^{+1.18} _{-1.42}	1.13	0.92	1.03
ESO ₃ 62mG18	60201046002	7.42	31.40 ^{+56.00} _{-11.42}	4.17 ^{+1.48} _{-2.40}	0.04	0.02	1.02
1RXSJ073308d7p455511	60260007002	8.36	10.21 ^{+211.31} _{-3.65}	7.27 ^{+2.24} _{-4.47}	0.01	0.00	1.18
SDSSJ114921d52p532013d4	60260009002	8.61	6.42 ^{+4.08} _{-1.73}	9.01 ^{+2.42} _{-2.94}	0.51	0.02	1.08
2MASXJ10195855m0234363	60260015002	8.34	33.03 ^{+286.33} _{-28.04}	3.02 ^{+15.18} _{-2.45}	0.05	0.00	1.24
AM0224m283	60363002002	7.91	13.39 ^{+59.67} _{-5.49}	5.45 ^{+2.30} _{-2.99}	0.27	0.05	0.84
2MASXJ19301380p3410495	60376001002	8.15	11.79 ^{+3.28} _{-2.02}	9.03 ^{+1.79} _{-1.52}	0.44	0.05	1.07
UGC06728	60376007002	5.66	33.26 ^{+46.56} _{-14.67}	3.24 ^{+1.42} _{-1.77}	0.01	0.45	1.04
Mrk590	90201043002	7.57	16.22 ^{+137.77} _{-6.44}	5.38 ^{+2.02} _{-3.68}	0.05	0.02	1.11

Table 4.3: The sample source that plasma temperature is lower limit

Name	Obs ID	Mass	kt	τ	L_{2-10}	λ_{EDD}	χ^2/dof
		$\log(M_{BH}/M_{\odot})$	keV		$\times 10^{44} \text{ erg/s}$		
3C382	60001084002	8.19	77.57 ^{+189.86}	1.17 _{-0.43}	2.55	0.26	1.02
Fairall ₉	60001130003	8.3	76.45 ^{+76.90}	0.50 _{-0.50}	1.25	0.10	0.94
NGC3516	60002042004	7.39	89.08 ^{+404.91}	0.86 _{-0.30}	0.01	0.01	1.07
RBS0770	60061092002	7.34	57.59 ^{+303.67}	1.83 _{-0.19}	0.55	0.40	0.93
RBS1125	60061229002	7.76	23.03 ^{+51.56}	1.25 _{-0.76}	0.47	0.13	1.02
IJRJ14471m6414	60061257002	7.7	16.94 ^{+483.06}	5.76 _{-0.10}	0.32	0.10	1.09
S52116p81	60061303002	8.9	19.11 ^{+182.16}	4.46 _{-0.49}	2.58	0.05	0.96
3C227	60061329002	8.61	23.36 ^{+457.45}	1.60 _{-0.15}	2.52	0.10	1.00
MCGp01m57m016	60061343002	7.61	17.45 ^{+26.12}	5.18 _{-1.91}	0.07	0.03	1.08
2MASXJ12055599p4959561	60061357002	8.42	57.35 ^{+440.35}	2.93 _{-0.06}	0.18	0.01	1.25
Mrk841	60101023002	7.81	31.60 ^{+162.90}	2.72 _{-0.50}	0.58	0.14	0.95
Mrk1044	60160109002	6.44	20.51 ^{+45.15}	2.18 _{-1.16}	0.05	0.31	1.02
HB89 ₀ 241p622	60160125002	8.09	84.34 ^{+321.13}	1.18 _{-0.21}	1.16	0.15	1.05
PKS0558m504	60160254002	7.33	10.03 ^{+11.90}	1.84 _{-2.72}	5.65	4.20	0.86
PG0804+761	60160322002	8.73	45.65 ^{+246.60}	2.28 _{-0.17}	2.02	0.06	0.96
Mrk817	60160590002	7.59	86.39 ^{+411.48}	0.72 _{-0.04}	0.25	0.10	0.98
2E1739d1m1210	60160670002	7.79	43.84 ^{+263.12}	1.43 _{-0.21}	0.38	0.10	1.04
2MASXiJ1802473m145454	60160680002	7.76	48.12 ^{+228.49}	3.32 _{-0.32}	0.72	0.20	1.03
2MASXJ19380437m5109497	60160716002	7.23	57.68 ^{+27.14}	4.91 _{-1.16}	0.34	0.32	0.91
2MASXJ20350566p2603301	60160741002	7.08	7.63 ^{+7.30}	3.02 _{-5.34}	0.22	0.29	1.07
2MASXJ04293830m2109441	60260006002	8.82	9.11 ^{+17.71}	4.09 _{-4.19}	0.19	0.00	1.10
6dFJ1254564m265702	60363001002	8.25	52.45 ^{+423.10}	3.49 _{-0.25}	0.50	0.04	0.93

Bibliography

- Arnaud, K. A. (1996). XSPEC: The First Ten Years. In Jacoby, G. H. and Barnes, J., editors, *Astronomical Data Analysis Software and Systems V*, volume 101 of *Astronomical Society of the Pacific Conference Series*, page 17.
- Bañados, E., Venemans, B. P., Mazzucchelli, C., Farina, E. P., Walter, F., Wang, F., Decarli, R., Stern, D., Fan, X., and Davies, F. B. (2018). An 800-million-solar-mass black hole in a significantly neutral Universe at a redshift of 7.5. , 553(7689):473–476.
- Baumgartner, W. H., Tueller, J., Markwardt, C. B., Skinner, G. K., Barthelmy, S., Mushotzky, R. F., Evans, P. A., and Gehrels, N. (2013). THE 70 MONTHSWIFT-BAT ALL-SKY HARD x-RAY SURVEY. *The Astrophysical Journal Supplement Series*, 207(2):19.
- Bentz, M. C. and Katz, S. (2015). The AGN Black Hole Mass Database. , 127:67.
- Blumenthal, G. R. and Gould, R. J. (1970). Bremsstrahlung, Synchrotron Radiation, and Compton Scattering of High-Energy Electrons Traversing Dilute Gases. *Reviews of Modern Physics*, 42:237–271.
- Chartas, G., Kochanek, C. S., Dai, X., Poindexter, S., and Garmire, G. (2009). X-Ray Microlensing in RXJ1131-1231 and HE1104-1805. , 693:174–185.
- Dadina, M. (2007). BeppoSAX observations in the 2-100 keV band of the nearby Seyfert galaxies: an atlas of spectra. , 461(3):1209–1252.
- Dadina, M. (2008). Seyfert galaxies in the local Universe ($z \leq 0.1$): the average X-ray spectrum as seen by BeppoSAX. , 485(2):417–424.
- de Rosa, A., Panessa, F., Bassani, L., Bazzano, A., Bird, A., Landi, R., Malizia, A., Molina, M., and Ubertini, P. (2012). Broad-band study of hard X-ray-selected absorbed active galactic nuclei. , 420:2087–2101.
- Fabian, A., Zoghbi, A., Ross, R., Uttley, P., Gallo, L., Brandt, W., Blustin, A., Boller, T., Caballero-Garcia, M., Larsson, J., Miller, J., Miniutti, G., Ponti, G., Reis, R., Reynolds, C., Tanaka, Y., and Young, A. (2009). Broad line emission from iron k- and l-shell transitions in the active galaxy 1h0707-495. *Nature*, 459:540–2.
- Fabian, A. C., Lohfink, A., Belmont, R., Malzac, J., and Coppi, P. (2017). Properties of AGN coronae in the NuSTAR era - II. Hybrid plasma. , 467:2566–2570.

Bibliography

- Fabian, A. C., Lohfink, A., Kara, E., Parker, M. L., Vasudevan, R., and Reynolds, C. S. (2015). Properties of AGN coronae in the NuSTAR era. *Monthly Notices of the Royal Astronomical Society*, 451(4):4375–4383.
- Gehrels, N., Chincarini, G., Giommi, P., Mason, K. O., Nousek, J. A., Wells, A. A., White, N. E., Barthelmy, S. D., Burrows, D. N., Cominsky, L. R., Hurley, K. C., Marshall, F. E., Meszaros, P., Roming, P. W. A., Angelini, L., Barbier, L. M., Belloni, T., Campana, S., Caraveo, P. A., Chester, M. M., Citterio, O., Cline, T. L., Cropper, M. S., Cummings, J. R., Dean, A. J., Feigelson, E. D., Fenimore, E. E., Frail, D. A., Fruchter, A. S., Garmire, G. P., Gendreau, K., Ghisellini, G., Greiner, J., Hill, J. E., Hunsberger, S. D., Krimm, H. A., Kulkarni, S. R., Kumar, P., Lebrun, F., Lloyd-Ronning, N. M., Markwardt, C. B., Mattson, B. J., Mushotzky, R. F., Norris, J. P., Osborne, J., Paczynski, B., Palmer, D. M., Park, H.-S., Parsons, A. M., Paul, J., Rees, M. J., Reynolds, C. S., Rhoads, J. E., Sasseen, T. P., Schaefer, B. E., Short, A. T., Smale, A. P., Smith, I. A., Stella, L., Tagliaferri, G., Takahashi, T., Tashiro, M., Townsley, L. K., Tueller, J., Turner, M. J. L., Vietri, M., Voges, W., Ward, M. J., Willingale, R., Zerbi, F. M., and Zhang, W. W. (2004). TheSwiftGamma-ray burst mission. *The Astrophysical Journal*, 611(2):1005–1020.
- Greene, J. E. and Ho, L. C. (2005). Estimating Black Hole Masses in Active Galaxies Using the H α Emission Line. , 630(1):122–129.
- Guilbert, P. W., Fabian, A. C., and Rees, M. J. (1983). Spectral and variability constraints on compact sources. *Monthly Notices of the Royal Astronomical Society*, 205(3):593–603.
- Haardt, F. and Maraschi, L. (1993). X-ray spectra from two-phase accretion disks. , 413:507–517.
- Harrison, F. A., Craig, W. W., Christensen, F. E., Hailey, C. J., Zhang, W. W., Boggs, S. E., Stern, D., Cook, W. R., Forster, K., Giommi, P., Grefenstette, B. W., Kim, Y., Kitaguchi, T., Koglin, J. E., Madsen, K. K., Mao, P. H., Miyasaka, H., Mori, K., Perri, M., Pivovarov, M. J., Puccetti, S., Rana, V. R., Westergaard, N. J., Willis, J., Zoglauer, A., An, H., Bachetti, M., Barrière, N. M., Bellm, E. C., Bhalerao, V., Brejnholt, N. F., Fuerst, F., Liebe, C. C., Markwardt, C. B., Nynka, M., Vogel, J. K., Walton, D. J., Wik, D. R., Alexander, D. M., Cominsky, L. R., Hornschemeier, A. E., Hornstrup, A., Kaspi, V. M., Madejski, G. M., Matt, G., Molendi, S., Smith, D. M., Tomsick, J. A., Ajello, M., Ballantyne, D. R., Baloković, M., Barret, D., Bauer, F. E., Blandford, R. D., Brandt, W. N., Brenneman, L. W., Chiang, J., Chakrabarty, D., Chenevez, J., Comastri, A., Dufour, F., Elvis, M., Fabian, A. C., Farrah, D., Fryer, C. L., Gotthelf, E. V., Grindlay, J. E., Helfand, D. J., Krivonos, R., Meier, D. L., Miller, J. M., Natalucci, L., Ogle, P., Ofek, E. O., Ptak, A., Reynolds, S. P., Rigby, J. R., Tagliaferri, G., Thorsett, S. E., Treister, E., and Urry, C. M. (2013). The Nuclear Spectroscopic Telescope Array (NuSTAR) High-energy X-Ray Mission. , 770:103.

Bibliography

- Hua, X.-M. and Titarchuk, L. (1995). Comptonization Models and Spectroscopy of X-Ray and Gamma-Ray Sources: A Combined Study by Monte Carlo and Analytical Methods. , 449:188.
- Kamraj, N., Harrison, F. A., Baloković, M., Lohfink, A., and Brightman, M. (2018). Coronal Properties of Swift/BAT-selected Seyfert 1 AGNs Observed with NuSTAR. , 866:124.
- Kormendy, J. and Ho, L. C. (2013). Coevolution (Or Not) of Supermassive Black Holes and Host Galaxies. , 51(1):511–653.
- Koss, M., Trakhtenbrot, B., Ricci, C., Lamperti, I., Oh, K., Berney, S., Schawinski, K., Baloković, M., Baronchelli, L., Crenshaw, D. M., Fischer, T., Gehrels, N., Harrison, F., Hashimoto, Y., Hogg, D., Ichikawa, K., Masetti, N., Mushotzky, R., Sartori, L., Stern, D., Treister, E., Ueda, Y., Veilleux, S., and Winter, L. (2017). BAT AGN Spectroscopic Survey. I. Spectral Measurements, Derived Quantities, and AGN Demographics. , 850:74.
- Lasota, J.-P. (2016). Black Hole Accretion Discs. In Bambi, C., editor, *Astrophysics of Black Holes: From Fundamental Aspects to Latest Developments*, volume 440 of *Astrophysics and Space Science Library*, page 1.
- Longair, M. (2011). *High Energy Astrophysics*. Cambridge University Press.
- Magdziarz, P. and Zdziarski, A. A. (1995). Angle-dependent Compton reflection of X-rays and gamma-rays. , 273:837–848.
- Malizia, A., Molina, M., Bassani, L., Stephen, J. B., Bazzano, A., Ubertini, P., and Bird, A. J. (2014). The INTEGRAL High-energy Cut-off Distribution of Type 1 Active Galactic Nuclei. , 782(2):L25.
- Mason, R. E. (2015). Dust in the torus of the AGN unified model. , 116:97–101.
- Merloni, A. and Fabian, A. C. (2001). Accretion disc coronae as magnetic reservoirs. *Monthly Notices of the Royal Astronomical Society*, 321(3):549–552.
- Morrison, R. and McCammon, D. (1983). Interstellar photoelectric absorption cross sections, 0.03-10 keV. , 270:119–122.
- Padovani, P., Alexander, D. M., Assef, R. J., De Marco, B., Giommi, P., Hickox, R. C., Richards, G. T., Smolčić, V., Hatziminaoglou, E., and Mainieri, V. (2017). Active galactic nuclei: what’s in a name? , 25(1):2.
- Petrucci, P. O., Haardt, F., Maraschi, L., Grandi, P., Malzac, J., Matt, G., Nicastro, F., Piro, L., Perola, G. C., and Rosa, A. D. (2001). Testing comptonization models Using BeppoSAX Observations of seyfert 1 galaxies. *The Astrophysical Journal*, 556(2):716–726.

Bibliography

- Ramos Almeida, C. and Ricci, C. (2017). Nuclear obscuration in active galactic nuclei. *Nature Astronomy*, 1:679–689.
- Ricci, C., Ho, L. C., Fabian, A. C., Trakhtenbrot, B., Koss, M. J., Ueda, Y., Lohfink, A., Shimizu, T., Bauer, F. E., Mushotzky, R., Schawinski, K., Paltani, S., Lamperti, I., Treister, E., and Oh, K. (2018). BAT AGN Spectroscopic Survey - XII. The relation between coronal properties of active galactic nuclei and the Eddington ratio. , 480:1819–1830.
- Ricci, C., Trakhtenbrot, B., Koss, M. J., Ueda, Y., Del Vecchio, I., Treister, E., Schawinski, K., Paltani, S., Oh, K., Lamperti, I., Berney, S., Gandhi, P., Ichikawa, K., Bauer, F. E., Ho, L. C., Asmus, D., Beckmann, V., Soldi, S., Baloković, M., Gehrels, N., and Markwardt, C. B. (2017). BAT AGN Spectroscopic Survey. V. X-Ray Properties of the Swift/BAT 70-month AGN Catalog. , 233(2):17.
- Rybicki, G. B. and Lightman, A. P. (1986). *Radiative Processes in Astrophysics*.
- Shestakov, A., S. Kershaw, D., and Prasad, M. (1988). Evaluation of integrals of the Compton scattering cross-section. *Journal of Quantitative Spectroscopy & Radiative Transfer - J QUANT SPECTROSC RADIAT*, 40:577–589.
- Sunyaev, R. A. and Titarchuk, L. G. (1980). Comptonization of X-rays in plasma clouds - Typical radiation spectra. , 86:121–138.
- Svensson, R. (1984). Steady mildly relativistic thermal plasmas - Processes and properties. , 209:175–208.
- Titarchuk, L. (1994). Generalized Comptonization models and application to the recent high-energy observations. , 434:570–586.
- Tortosa, A., Bianchi, S., Marinucci, A., Matt, G., and Petrucci, P. O. (2018). A NuSTAR census of coronal parameters in Seyfert galaxies. , 614:A37.
- Trakhtenbrot, B. and Netzer, H. (2012). Black hole growth to $z = 2$ - I. Improved virial methods for measuring M_{BH} and L/L_{Edd} . , 427(4):3081–3102.
- Vasudevan, R. V. and Fabian, A. C. (2009). Simultaneous X-ray/optical/UV snapshots of active galactic nuclei from XMM-Newton: spectral energy distributions for the reverberation mapped sample. , 392:1124–1140.
- Zier, C. and Biermann, P. L. (2002). Binary black holes and tori in AGN. II. Can stellar winds constitute a dusty torus? , 396:91–108.